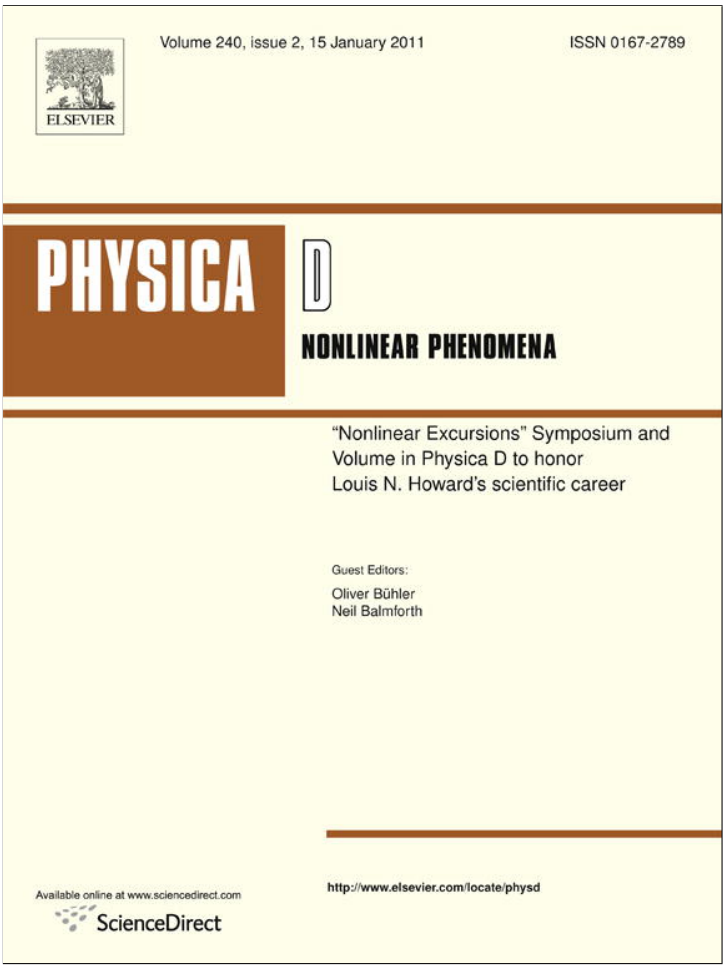

Physica D 240 (2011) 212–232

Contents lists available at ScienceDirect

Physica D

journal homepage: www.elsevier.com/locate/physd

Hamiltonian–Dirac simulated annealing: Application to the calculation of vortex states

G.R. Flierl [a], P.J. Morrison [b,*]

[a] Department of Earth, Atmospheric, and Planetary Sciences, Massachusetts Institute of Technology, Cambridge, MA 02139-4307, USA

[b] Department of Physics and Institute for Fusion Studies, The University of Texas at Austin, Austin, TX, 78712, USA

ARTICLE INFO

Article history:
Available online 22 September 2010

Keywords:
Vortex dynamics
Hamiltonian
Noncanonical Poisson bracket
Lie–Poisson bracket
Dirac bracket
Simulated annealing

ABSTRACT

A simulated annealing method for calculating stationary states for models that describe continuous media is proposed. The method is based on the noncanonical Poisson bracket formulation of media, which is used to construct Dirac brackets with desired constraints, and symmetric brackets that cause relaxation with the desired constraints. The method is applied to two-dimensional vortex dynamics and a variety of numerical examples is given, including the calculation of monopole and dipole vortex states.

1. Introduction

The Eulerian description of media has a Hamiltonian formulation in terms of noncanonical Poisson brackets (see [1–6] and references therein), brackets that are not of the standard form because Eulerian variables are not canonical variables. Incorporating dissipation into some kind of general formalism dates to Rayleigh, but the use of symmetric brackets in conjunction with noncanonical Poisson brackets for this purpose was proposed in [7–9]. Unlike the widely studied but more simplistic Cahn–Hilliard gradient flows (see e.g. [10]), the formulation of these authors was concerned with brackets that generate a dynamics compatible with the laws of thermodynamics, a formulation that was termed metriplectic dynamics in [11]. These systems are complete in the sense that energy is conserved while entropy is produced. Dissipative brackets have also been suggested for incomplete systems that have no notion of entropy but dissipate energy while preserving Casimir invariants [12–15]. See [16] for a general discussion. The latter were proposed as a means for computation, particularly [13–15] in the context of fluid mechanics, where the formalism was used and proposed for calculating stationary vortex states by a kind of simulated annealing dynamics.

We offer a new twist that overcomes difficulties obtained in [13–15]—we extremize energy at fixed Casimir invariants by using Dirac brackets to enforce constraints. In this way one can generate dynamics that is an energy extremizing rearrangement, while preserving additional properties such as linear or angular momentum. Here, this is done for a variety of numerical examples in the context of vortex dynamics. A preliminary version of our method was reported in [17] where some results for contour dynamics calculations were presented.

The paper is organized as follows: in Section 2 we develop the needed theory, which includes a description of the various bracket formulations. The specific case of two-dimensional vortex dynamics is used to illustrate the general ideas. This is followed in Section 3 by numerical examples that illustrate various kinds of dynamics, including vortex states with two-fold and three-fold symmetry and dipole states. In Section 4 two-layer quasigeostropic dynamics is considered with monopolar vorticity in each layer. Finally, in Section 5 we conclude.

2. Theory

As mentioned in Section 1, the theory behind our formulation has several basic parts: a noncanonical Poisson bracket defined on functionals or observables (see e.g. [2,6,18]), a Dirac bracket based on such a noncanonical Poisson bracket (see e.g. [19,20] for traditional Dirac brackets and see e.g. [17,21] for the noncanonical version), and a symmetric bracket that gives rise to relaxation akin to collision operators in kinetic theory (see e.g. [15,16]). We describe these objects here.

2.1. Functionals

Functionals map a set of dynamical variables into numbers. In general one may have M dynamical variables denoted by $\chi^i(z)$,

* Corresponding author. Tel.: +1 512 471 1527.
E-mail addresses: glenn@lake.mit.edu (G.R. Flierl), morrison@physics.utexas.edu (P.J. Morrison).

0167-2789/$ – see front matter © 2010 Elsevier B.V. All rights reserved.
doi:10.1016/j.physd.2010.08.011

where $i = 1, 2, \ldots, M$, that are functions of $z = (z^1, z^2, \ldots, z^N)$, coordinates for an N-dimensional domain, $\mathcal{D}$, and functionals of these variables will be denoted by $F[\chi]$.

For example, when the dynamical variable is a single vorticity-like variable, the case for the calculations of Section 3, the functional $F[q]$ maps the function $q(\mathbf{x})$ into $\mathbb{R}$. Here $\mathbf{x} = (x, y)$ is a point in $\mathcal{D}$, a planar region, taken for the numerical calculations here to be a 2-torus. Examples of such observables include the angular momentum,

$$L = -\frac{1}{2}\int_{\mathcal{D}} \mathrm{d}\mathbf{x}\, |\mathbf{x}|^2 q(\mathbf{x}), \tag{1}$$

and the Hamiltonian functional,

$$H = -\frac{1}{2}\int_{\mathcal{D}} \mathrm{d}\mathbf{x} \int_{\mathcal{D}} \mathrm{d}\mathbf{x}'\, q(\mathbf{x})\mathcal{G}(\mathbf{x}, \mathbf{x}')q(\mathbf{x}'), \tag{2}$$

where $\mathcal{G}$ is the relevant Green's function; for two-dimensional vorticity dynamics it satisfies $\nabla^2\mathcal{G}(\mathbf{x}) = \delta(\mathbf{x})$.

Note, the kinetic energy of the fluid on an infinite domain can have an infinite part associated with the $1/r$ far-field when the net vorticity is non-zero; since the latter is conserved, this component of the energy is fixed. Subtracting it from the total gives the Hamiltonian, which thus is not quite the physical energy. A similar situation arises for the angular momentum where a boundary term is removed from the quantity L. In the following we will refer to H as the energy and L as the angular momentum.

In addition to the functionals (1) and (2), there is $q(\mathbf{x}_0)$, the functional that is the evaluation of q at a particular point of its domain,

$$q(\mathbf{x}_0) = \int_{\mathcal{D}} \mathrm{d}\mathbf{x}\, \delta(\mathbf{x}_0 - \mathbf{x})q(\mathbf{x}). \tag{3}$$

This latter functional is needed when casting the equations of motion into Hamiltonian form, as is done in Section 2.5 below.

The time rate of change of functionals will be generated by making use of various brackets, and these involve a notion of functional or variational derivative. This kind of derivative describes how the value of the functional changes as we make small changes to its argument. Thus we consider the first variation,

$$\delta F[\chi; \eta] = \frac{\mathrm{d}}{\mathrm{d}\epsilon} F[\chi + \epsilon\eta]\bigg|_{\epsilon=0} = \int_{\mathcal{D}} \mathrm{d}^N z\, \frac{\delta F[\chi]}{\delta \chi^i}\eta^i, \tag{4}$$

where repeated indices are to be summed here (and will be henceforth unless otherwise stated). Using the integral over z as an inner product, the quantity $\delta F/\delta\chi$ can be interpreted as a gradient and $\delta F[\chi; \eta]$ as the Fréchet derivative acting on $\eta(z)$.

From this definition, the functional derivatives of the examples (1)–(3), are readily obtained,

$$\frac{\delta L[q]}{\delta q} = -\frac{|\mathbf{x}|^2}{2}, \tag{5}$$

$$\frac{\delta H[q]}{\delta q} = -\int_{\mathcal{D}} \mathrm{d}\mathbf{x}'\, \mathcal{G}(\mathbf{x}, \mathbf{x}')q(\mathbf{x}'), \tag{6}$$

$$\frac{\delta q(\mathbf{x}_0)}{\delta q} = \delta(\mathbf{x}_0 - \mathbf{x}), \tag{7}$$

where in (6) the symmetric nature of $\mathcal{G}$ has been used. With the streamfunction ψ that satisfies, $\nabla^2\psi = q$, we can write

$$\psi(\mathbf{x}) = \int_{\mathcal{D}} \mathrm{d}\mathbf{x}'\, \mathcal{G}(\mathbf{x}, \mathbf{x}')q(\mathbf{x}'), \tag{8}$$

and therefore the functional derivative of the Hamiltonian is

$$\frac{\delta H[q]}{\delta q(\mathbf{x})} = -\psi(\mathbf{x}). \tag{9}$$

Clearly the functional derivative depends in general upon spatial location—at times we will need to be explicit about this to distinguish $\mathbf{x}$ from $\mathbf{x}'$ etc.; therefore, we will use the notation

$$\frac{\delta F[q]}{\delta q(\mathbf{x})},$$

explicitly showing that the independent variable is $\mathbf{x}$. Thus (7) takes the perspicuous form

$$\frac{\delta q(\mathbf{x}_0)}{\delta q(\mathbf{x})} = \delta(\mathbf{x}_0 - \mathbf{x}),$$

a quantity that will be needed in the evaluation of Poisson brackets below.

2.2. Noncanonical Poisson brackets

A general noncanonical Poisson bracket is a binary operator on functionals of the form

$$\{F, G\} = \int_{\mathcal{D}} \mathrm{d}^N z' \int_{\mathcal{D}} \mathrm{d}^N z''\, \frac{\delta F[\chi]}{\delta \chi^i(z')}\mathbb{J}^{ij}(z', z'')\frac{\delta G[\chi]}{\delta \chi^j(z'')}, \tag{10}$$

where χ denotes a set of dynamical variables with M elements, $i, j = 1, \ldots, M$, that depends on a coordinate z of a space of dimension N. In (10), $\mathbb{J}$ is the cosymplectic operator that must ensure that the bracket satisfies: antisymmetry, $\{F, G\} = -\{G, F\}$, and the Jacobi identity, $\{\{F, G\}, H\} + \{\{G, H\}, F\} + \{\{H, F\}, G\} = 0$, for all functionals F, G, H. Note that, because of the form of (10), bilinearity and the Leibnitz derivation properties are manifest. It is not required that $\mathbb{J}$ be nondegenerate. When it is degenerate, i.e. has a nontrivial null space, there exist Casimir invariants, C, that satisfy $\{C, G\} = 0$ for all functionals G. (See e.g. [6,17] for review.)

The Poisson bracket for vortex dynamics [22,2,23] is the following:

$$\{F, G\} = \int_{\mathcal{D}} \mathrm{d}\mathbf{x}'\, q(\mathbf{x}')\left[\frac{\delta F[q]}{\delta q(\mathbf{x}')}, \frac{\delta G[q]}{\delta q(\mathbf{x}')}\right], \tag{11}$$

where $[A, B] = \hat{z}\cdot\nabla A \times \nabla B$ with $\hat{z}$ a unit vector normal to the planar region; thus, $[A, B]$ is an ordinary bracket that can be written in Cartesian components, or it can be written in terms of whatever the independent variables might be. For this example the cosymplectic operator $\mathbb{J} = -[q, \cdot]$ and the Jacobi identity can be proved directly by the techniques described in [2]. The well-known quantities $C[q] = \int_{\mathcal{D}} \mathrm{d}\mathbf{x}\, \mathcal{C}(q)$ with $\mathcal{C}$ arbitrary, a family of integrals that includes the net vorticity and enstrophy, are Casimir invariants. It is easy to show $\{C, G\} = 0$ for all G.

Dynamics is generated from the noncanonical Poisson bracket according to

$$\frac{\partial q}{\partial t} = \{q, H\}, \tag{12}$$

the usual Poisson bracket Hamiltonian form. We will refer to this dynamics as H-dynamics. With (7) and (11), we can show that

$$\begin{aligned}\{q(\mathbf{x}), G\} &= \int_{\mathcal{D}} \mathrm{d}\mathbf{x}'\, q(\mathbf{x}')\left[\frac{\delta q(\mathbf{x})}{\delta q(\mathbf{x}')}, \frac{\delta G[q]}{\delta q(\mathbf{x}')}\right] \\ &= \int_{\mathcal{D}} \mathrm{d}\mathbf{x}'\, q(\mathbf{x}')\left[\delta(\mathbf{x} - \mathbf{x}'), \frac{\delta G[q]}{\delta q(\mathbf{x}')}\right] \\ &= -\left[q(\mathbf{x}), \frac{\delta G[q]}{\delta q(\mathbf{x})}\right],\end{aligned} \tag{13}$$

using the identity $\int_{\mathcal{D}} \mathrm{d}\mathbf{x} f[g, h] = -\int_{\mathcal{D}} \mathrm{d}\mathbf{x}\, g[f, h]$, obtained by integration by parts and neglect of surface terms. We now have

$$\frac{\partial}{\partial t}q(\mathbf{x}) = \{q(\mathbf{x}), H\} = -\left[q(\mathbf{x}), \frac{\delta H[q]}{\delta q(\mathbf{x})}\right] = [q, \psi], \tag{14}$$

which is the usual form for the two-dimensional Euler equations. Functionals evolve according to

$$\frac{\partial F}{\partial t} = \{F, H\}; \tag{15}$$

since $\{C, H\} = 0$ for the Casimir invariants, they are indeed constant in time for any choice of the Hamiltonian.

2.3. Noncanonical Dirac brackets

From any bracket of the form of (10) and any choice of constraint functionals C_i such that the antisymmetric matrix $\{C_i, C_j\}$ is nonsingular, one can construct a generalized Dirac bracket as follows:

$$\{F, G\}_D = \{F, G\} - \{F, C_i\}\mathbb{C}^{ij}\{C_j, G\}, \tag{16}$$

where $\mathbb{C}^{ij} := \{C_i, C_j\}^{-1}$. Eq. (16) defines a bracket that is obviously antisymmetric and can be proven to satisfy the Jacobi identity (cf. Appendix C of [21]). Under this form, the constraints C_i, are Casimir invariants,

$$\{C_i, G\}_D = 0 \quad \text{for all } G. \tag{17}$$

For the matrix $\{C_i, C_j\}$ to be invertible, we must have an even number of constraints, and none of the C_i's can be Casimir invariants of the original noncanonical bracket; to distinguish those from the ones used in the Dirac construction, we will refer to the latter as Dirac constraints.

Dirac constructed such brackets out of canonical Poisson brackets with the goal of quantizing classical field theories, but here we use noncanonical Poisson brackets, and the aim is the purely classical imposition of constraints on the dynamics. Although one can construct Dirac brackets out of any even number of constraints, we will generally use only two or four global constraints, i.e. ones that involve integration and do not depend explicitly on z. For pointwise constraints, $C_i(z)$, the general bracket has the following form:

$$\{F, G\}_D = \{F, G\} - \int_{\mathcal{D}} \mathrm{d}^N z' \int_{\mathcal{D}} \mathrm{d}^N z'' \times \{F, C_i(z')\}\mathbb{C}^{ij}(z', z'')\{C_j(z''), G\}.$$

We will refer to dynamics generated by Dirac brackets as HD-dynamics.

For the numerical examples treated in Sections 3 and 4 we will use global Dirac constraints of linear form,

$$C_i = \int_{\mathcal{D}} \mathrm{d}\mathbf{x}\, c_i(\mathbf{x}) q(\mathbf{x}), \tag{18}$$

where the c_i and the initial condition will be chosen by intuition and by considering the desired symmetries of the final state. With this form for the Dirac constraints, the Dirac bracket is readily evaluated using $\delta C_i/\delta q(\mathbf{x}) = c_i(\mathbf{x})$ which gives e.g.

$$\{C_i, C_j\} = \int_{\mathcal{D}} \mathrm{d}\mathbf{x}\, q[c_i, c_j] \quad \text{and} \quad \{F, C_i\} = \int_{\mathcal{D}} \mathrm{d}\mathbf{x}\, q\left[\frac{\delta F}{\delta q}, c_i\right].$$

In the case of two constraints, the required matrix is simple:

$$\mathbb{C} = \begin{pmatrix} 0 & -1/\{C_1, C_2\} \\ 1/\{C_1, C_2\} & 0 \end{pmatrix}. \tag{19}$$

To generate dynamics, we note that for a global functional G, the term

$$A^i = \mathbb{C}^{ij}\{C_j, G\} \tag{20}$$

is, at most, a function of time but not $\mathbf{x}$. Therefore from

$$\{F, G\}_D = \{F, G\} - A^i\{F, C_i\}, \tag{21}$$

we see that the evolution of F under (11) is given by

$$\{F, G\}_D = \int_{\mathcal{D}} \mathrm{d}\mathbf{x}\, q\left[\frac{\delta F}{\delta q}, \frac{\delta G}{\delta q}\right] - A^i \int_{\mathcal{D}} \mathrm{d}\mathbf{x}\, q\left[\frac{\delta F}{\delta q}, \frac{\delta C_i}{\delta q}\right] = \int_{\mathcal{D}} \mathrm{d}\mathbf{x}\, q\left[\frac{\delta F}{\delta q}, \frac{\delta G}{\delta q} - A^i\frac{\delta C_i}{\delta q}\right]. \tag{22}$$

Thus, the flow develops according to

$$\frac{\partial}{\partial t} q = -[\Psi, q], \tag{23}$$

where

$$\Psi = \psi + A^i c_i \quad \text{and} \quad A^i = -\left(\int_{\mathcal{D}} \mathrm{d}\mathbf{x}\, q[c_i, c_j]\right)^{-1} \int_{\mathcal{D}} \mathrm{d}\mathbf{x}\, c_j[\psi, q]. \tag{24}$$

This form follows from $\{C_j, H\}$ using (11) or directly from

$$\{C_j, H\} = \frac{\partial}{\partial t} C_j = \int_{\mathcal{D}} \mathrm{d}\mathbf{x}\, c_j \frac{\partial}{\partial t} q.$$

Thus, Dirac bracket dynamics is the "advection" of q by Ψ, which is the usual streamfunction with the addition of the constraint fields multiplied by the time dependent coefficients A^i.

In Section 3 we will use the invariants $C_1 = -L$ and C_2 equal to the strain moment, defined by

$$S = \int_{\mathcal{D}} \mathrm{d}\mathbf{x}\, xy\, q. \tag{25}$$

With these choices we see that Ψ obtains a rotational piece multiplied by A_1, a global quantity, and a piece that is a straining field multiplied by A_2, also a global quantity, viz.

$$A_1 = \frac{\int_{\mathcal{D}} \mathrm{d}\mathbf{x}\, xy[\psi, q]}{\int_{\mathcal{D}} \mathrm{d}\mathbf{x}\, (x^2 - y^2)q} \quad \text{and} \quad A_2 = -\frac{\frac{1}{2}\int_{\mathcal{D}} \mathrm{d}\mathbf{x}\, (x^2 + y^2)[\psi, q]}{\int_{\mathcal{D}} \mathrm{d}\mathbf{x}\, (x^2 - y^2)q}. \tag{26}$$

The time dependence in the A^i applies the two fields in just the right combination to keep the C_i constant. Although the angular momentum is already conserved by vortex dynamics, this is not necessarily the case when quantities evolve according to Dirac brackets (cf. Section 3.1 and Appendix D of [21]). Choosing $-L$ as one of our Dirac constraints guarantees that it remains conserved.

Although (21) resembles the procedure suggested in [15] of adding terms to H with Lagrange multipliers, it is different in that the coefficients change in time to ensure that the Dirac constraints remain constant. Furthermore, at least one of the constraints must not be a constant of motion under the original dynamics to ensure that the vector $\{C_j, H\}$ is non-zero.

2.4. Symmetric brackets

A general symmetric bracket analogous to (10) is given by

$$((F, G))_{\mathbb{G}} = \int_{\mathcal{D}} \mathrm{d}^N z' \int_{\mathcal{D}} \mathrm{d}^N z'' \frac{\delta F[\chi]}{\delta \chi^i(z')} \mathbb{G}^{ij}(z', z'') \frac{\delta G[\chi]}{\delta \chi^j(z'')}, \tag{27}$$

where the metric operator $\mathbb{G}$ is chosen to ensure $((F, G))_{\mathbb{G}} = ((G, F))_{\mathbb{G}}$ and to be semidefinite. We may also want to build degeneracies into $\mathbb{G}$ so that there exist distinguished functionals D that satisfy $((D, G))_{\mathbb{G}} = 0$ for all G.

Here we will be interested in a specific form of (27) that is a generalization of the symmetric brackets given in previous work [11,13,15,16], viz.

$$((F,G)) = \int_{\mathcal{D}} \mathrm{d}^N z' \int_{\mathcal{D}} \mathrm{d}^N z'' \, \{F, \chi^i(z')\} \mathcal{K}_{ij}(z', z'') \{\chi^j(z''), G\}, \quad (28)$$

with $\mathcal{K}$ a definite symmetric kernel that can be chosen at will, e.g., to effect smoothing. With this form, the Casimir invariants of $\{F, G\}$ will automatically be distinguished functionals D. We will refer to dynamics involving this kind of bracket as SA-dynamics, where SA stands for simulated annealing.

The symmetric bracket of (28) can be even further generalized as follows:

$$((F,G))_D = \int_{\mathcal{D}} \mathrm{d}^N z' \int_{\mathcal{D}} \mathrm{d}^N z'' \{F, \chi^i(z')\}_D \mathcal{K}_{ij}(z', z'') \{\chi^j(z''), G\}_D, \quad (29)$$

which is of the form of (28) but with a Dirac bracket replacing $\{,\}$. When this is the case, the set of distinguished functionals will be the union of the Casimir invariants of the bracket $\{F, G\}$ with the Dirac constraints used in the construction of $\{F, G\}_D$. We will refer to dynamics generated by this kind of bracket as DSA-dynamics for Dirac simulated annealing dynamics.

If a Hamiltonian-like functional $\mathcal{F}$ is used to generate dynamics, then all three of the brackets (27)–(29) have the property $\mathrm{d}\mathcal{F}/\mathrm{d}t \geq 0$. For example, under SA dynamics,

$$\frac{\mathrm{d}\mathcal{F}}{\mathrm{d}t} = \alpha((\mathcal{F}, \mathcal{F})) \geq 0, \quad (30)$$

when $\mathcal{K}_{ij}$ is negative and α, a parameter that measures the 'dissipative' time scale, is positive. This inequality follows from the symmetry built into the bracket. In fact, the sign of α can be chosen to make the dynamics minimize or maximize $\mathcal{F}$. Thus we have a formal 'H-theorem', akin to that of the Boltzmann equation, and the rudiments for possibly building rigorous theorems about asymptotic stability.

For our vortex example with the H of (2),

$$\begin{aligned}((q(\mathbf{x}), H)) &= \int_{\mathcal{D}} \mathrm{d}\mathbf{x}' \int_{\mathcal{D}} \mathrm{d}\mathbf{x}'' \, \{q(\mathbf{x}), q(\mathbf{x}')\} \mathcal{K}(\mathbf{x}', \mathbf{x}'') \{q(\mathbf{x}''), H\} \\ &= -\int_{\mathcal{D}} \mathrm{d}\mathbf{x}' \, [\delta(\mathbf{x} - \mathbf{x}'), q(\mathbf{x}')] \\ &\quad \times \int_{\mathcal{D}} \mathrm{d}\mathbf{x}'' \, \mathcal{K}(\mathbf{x}', \mathbf{x}'') [q(\mathbf{x}''), \psi(\mathbf{x}'')] \\ &= [\Phi(\mathbf{x}), q(\mathbf{x})],\end{aligned}$$

where we have used (13) and (14) and defined an effective streamfunction by

$$\Phi(\mathbf{x}) = \int_{\mathcal{D}} \mathrm{d}\mathbf{x}' \, \mathcal{K}(\mathbf{x}, \mathbf{x}') [q(\mathbf{x}'), \psi(\mathbf{x}')]. \quad (31)$$

As pointed out in [13,14] for the special case where $\mathcal{K}(\mathbf{x}, \mathbf{x}') = \delta(\mathbf{x} - \mathbf{x}')$, the resulting dynamical equation is still an advective equation, but with an altered non-divergent flow field, so that q is conserved pointwise and all the moments of q are conserved. The specific form of inequality (30), which relies on the symmetry of $\mathcal{K}$, can be shown directly. We do so for the case when $\mathcal{K}$ is the Green's function $\mathcal{G}$ that satisfies $\nabla^2 \mathcal{G}(\mathbf{x}) = \delta(\mathbf{x})$. We obtain

$$\begin{aligned}((H,H)) &= -\int_{\mathcal{D}} \mathrm{d}\mathbf{x}' \, \Phi(\mathbf{x}') \{q(\mathbf{x}'), H\} \\ &= -\int_{\mathcal{D}} \mathrm{d}\mathbf{x}' \, \Phi(\mathbf{x}') [q(\mathbf{x}'), \psi(\mathbf{x}')] \\ &= -\int_{\mathcal{D}} \mathrm{d}\mathbf{x}' \, \Phi(\mathbf{x}') \nabla^2 \Phi(\mathbf{x}') = \int_{\mathcal{D}} \mathrm{d}\mathbf{x}' \, |\nabla \Phi(\mathbf{x}')|^2, \end{aligned} \quad (32)$$

using $\nabla^2 \Phi = [q, \psi]$. Therefore, because $((H,H)) \geq 0$, when $\alpha > 0$, H tends to maximize, while if $\alpha < 0$, H tends to minimize.

Finally, the DSA form is given by

$$((q(\mathbf{x}), H))_D = \int_{\mathcal{D}} \mathrm{d}\mathbf{x}' \, \{q(\mathbf{x}), q(\mathbf{x}')\}_D \Phi_D(\mathbf{x}') \quad (33)$$

with

$$\begin{aligned}\Phi_D(\mathbf{x}) &= \int_{\mathcal{D}} \mathrm{d}\mathbf{x}' \, \mathcal{K}(\mathbf{x}, \mathbf{x}') \{q(\mathbf{x}'), H\}_D \\ &= \int_{\mathcal{D}} \mathrm{d}\mathbf{x}' \, \mathcal{K}(\mathbf{x}, \mathbf{x}') [q(\mathbf{x}'), \psi(\mathbf{x}') + A^i c_i(\mathbf{x}')]. \end{aligned} \quad (34)$$

Using the definition of the Dirac bracket (16) and (13) gives

$$\begin{aligned}\{q(\mathbf{x}), q(\mathbf{x}')\}_D &= \{q(\mathbf{x}), q(\mathbf{x}')\} - \{q(\mathbf{x}), C_i\} \mathbb{C}^{ij} \{C_j, q(\mathbf{x}')\} \\ &= [q(\mathbf{x}'), \delta(\mathbf{x} - \mathbf{x}')] - [c_i(\mathbf{x}), q(\mathbf{x})] \mathbb{C}^{ij} [q(\mathbf{x}'), c_j(\mathbf{x}')].\end{aligned}$$

Therefore the DSA bracket becomes

$$\begin{aligned}((q(\mathbf{x}), H))_D &= [\Phi_D(\mathbf{x}), q(\mathbf{x})] + [B^i c_i(\mathbf{x}), q(\mathbf{x})] \\ &= [\Phi_D + B^i c_i, q] \end{aligned} \quad (35)$$

with

$$B^i = \mathbb{C}^{ij} \int_{\mathcal{D}} \mathrm{d}\mathbf{x}' \, c_j(\mathbf{x}') [q(\mathbf{x}'), \Phi_D(\mathbf{x}')]. \quad (36)$$

Again, the q field evolves by advection, with the 'flow' including corrections to maintain the Dirac constraints.

2.5. Various dynamics

Various kinds of dynamical systems that can be generated by the brackets described above are listed below:

$$\text{Hamiltonian: } \frac{\partial}{\partial t} F = \{F, \mathcal{F}\}, \quad (37)$$

$$\text{Hamiltonian Dirac: } \frac{\partial}{\partial t} F = \{F, \mathcal{F}\}_D, \quad (38)$$

$$\text{Simulated Annealing: } \frac{\partial}{\partial t} F = \sigma \{F, \mathcal{F}\} + \alpha((F, \mathcal{F})), \quad (39)$$

$$\text{Dirac Simulated Annealing: } \frac{\partial}{\partial t} F = \sigma \{F, \mathcal{F}\}_D + \alpha((F, \mathcal{F}))_D. \quad (40)$$

In these equations F represents an arbitrary observable and $\mathcal{F}$ is a single functional that is used to generate the time advancement. Eqs. (37) and (38) are ideal and conserve energy in principle, although this will not be precisely the case when numerically solved. In (39) and (40) the parameters σ and α can be used to weight the contributions of the ideal and dissipative dynamics, respectively. For our runs we will choose $\sigma \in \{0, 1\}$ and $\alpha \in \{-1, 1\}$. For the functional $\mathcal{F}$, we shall use the Hamiltonian, H, but remark that it can more generally be assumed to have the form

$$\mathcal{F} = H + \sum_i C_i + \lambda^i P_i, \quad (41)$$

where the Cs are Casimir invariants and the Ps are dynamical invariants that commute with the particular Hamiltonians H of interest—we also require that the Ps commute with any Dirac constraints employed. The presence of the Ps in $\mathcal{F}$ generates dynamics in moving frames. For example, if one adds the linear or angular momentum to H, then (39) generates dynamics in a uniformly translating or rotating frame, respectively. Consequently, extremal points of (41) are stationary states in moving frames. Unlike the Ps of (41), the H and the Dirac constraints in DSA-dynamics are used to hold the vortices in place.

With the above assumptions on $\mathcal{F}$, the dynamics generated by (37) clearly conserves all Casimir invariants for any H, and the

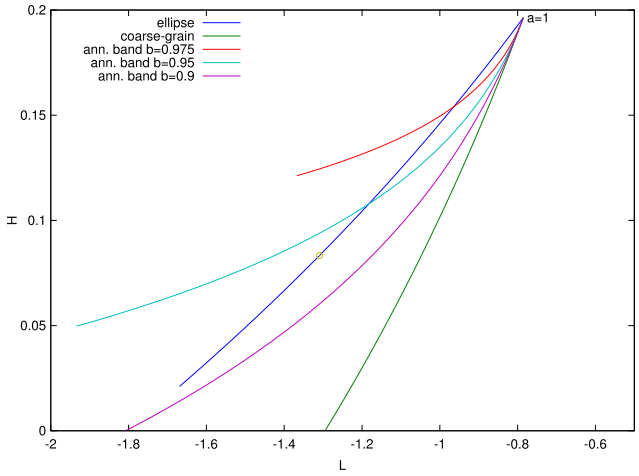

Fig. 1. H–L diagram showing the relationship between energy and angular momentum for various vortex states, including the Kirchhoff elliptical vortex parameterized by aspect ratio, a "coarse-grained" circular vortex parameterized by size, and a few vortices with a central core surrounded by an annular band also parameterized by size The point ○ marks the aspect ratio three stability threshold for the Kirchhoff ellipses.

H chosen is itself an invariant. Similarly, the dynamics generated by (38) conserves the Casimir invariants of $\{,\}$ and the Dirac constraints for any choice of H, and the chosen H (cf. [21]). It is well-known that finite degree-of-freedom Hamiltonian systems cannot have asymptotically stable fixed points, for this would violate Liouville's theorem. Thus, we do not expect (37) and (38) to possess asymptotically stable equilibria in any frame of reference. However, these systems are infinite-dimensional systems in which filamentation is known to occur (see e.g. Fig. 4). Filamentation gives rise to steep gradients and thus a small amount of dissipation can cause relaxation. Similarly, averaging over filamentation gives rise to relaxation by the mechanism of phase mixing, the essence of the Riemann–Lebesgue lemma and Landau damping. Thus, it will not be a surprise to see relaxation in our numerical experiments.

As noted in Section 2.4, by construction the dynamics of (39) and (40) conserve the Casimir invariants, and the latter conserves the imposed Dirac constraints, both for any Hamiltonian, H. However, the chosen H $\left(\text{or } H + \sum \lambda^i P_i\right)$ is no longer conserved but satisfies $\dot{H} \geq 0$ or $\dot{H} \leq 0$ depending on the sign of α. Therefore, H can serve as a Liapunov functional for asymptotic stability (see e.g. [24]). Thus as indicated in Section 1, these brackets give rise to dynamics that is an energy extremizing rearrangement subject to the Dirac constraints, and it is this dynamics that we find useful for numerically obtaining equilibrium states.

2.6. Kelvin's sponge

It is well-known in the calculus of variations that constraints are sometimes ineffective [25]. For vortex dynamics this situation may arise when one attempts to minimize energy at fixed Casimir invariants. As anticipated by Kelvin [26], vorticity invariants do not preclude the minimum zero energy state, but may produce a sponge-like structure with interpenetrating regions of vorticity (see [13] for another discussion and examples). Here we give a simple example that contains a central idea of when this effect occurs, an example we find useful for interpreting our numerical results.

Consider a real-valued function $u(x)$ defined on $[0, 2\pi]$. First, suppose we wish to maximize the 'energy' functional $H[u] = \int_0^{2\pi} \mathrm{d}x\, u^2$ subject to the constraint $C[u] = \int_0^{2\pi} \mathrm{d}x\, u_x^2 = C_0$, with the boundary conditions $u(0) = u(2\pi) = 0$. The variational problem $\delta(H - kC) = 0$ gives the Euler–Lagrange equation $ku_{xx} = -u$, and for $C_0 \neq 0$ it is easy to show that $k > 0$. The eigenvalues for this problem are $\lambda_n = 1/k_n = n^2$, where $n \in \mathbb{N}$, and the corresponding set of orthonormal eigenfunctions is composed of $u_n = \sin(nx)/\sqrt{\pi}$. Choosing $u = au_m$, for some $m \in \mathbb{N}$, gives $C_0 = a^2/k_m$, which determines a, and $H = C_0/\lambda_m$. Thus, the maximum value of H occurs for the smallest eigenvalue, $\lambda_1 = 1$. Had we chosen u to be a linear combination of two or more eigenfunctions, then it is not difficult to show the resulting value of H would be smaller. Thus, this example constitutes a well-defined extremization problem.

However, when we seek to minimize $H[u]$ subject to $C[u] = C_0$, we see that C plays no role. In this case we have the same Euler–Lagrange equation, eigenvalues, and eigenfunctions, but we wish to minimize $H = C_0/\lambda_m$. Because $\lambda_m = m^2$, with $m \in \mathbb{N}$, can be made arbitrarily large, $\inf H[u] = 0$, which is of course the minimum of $H[u]$ without the constraint C. A rule of thumb for minimum problems is that the constraint will only contribute if it contains fewer derivatives than the functional that is desired to be minimized and vice versa for maximum problems.

The simple maximum example above was chosen to represent the situation for vortex dynamics when the energy is maximized at fixed Casimir invariants. Thus it is not a surprise that SA-dynamics should produce nice circular vortex states, and this is evidenced by the successful numerical examples of [13,14]. However, if additional constraints are imposed one may obtain other states. For example, as stated in Section 2.5, it is known that equilibria in rotating frames are extrema of $H+\lambda L$ and thus, as suggested in [15], one might be able to use SA-dynamics to obtain nonaxisymmetric vortex states. In our tests this approach tended to be susceptible to either forming very thin ellipses, maximizing λL at the expense of H, or to creating a sponge-like structure, minimizing H at the expense of λL. We will see in Section 3 that we obtain better results by using DSA-dynamics with additional constraints.

As noted above, our simple minimization problem represents the situation of vortex energy minimization at constant Casimir invariants. The Casimir invariants are a consequence of the fact that vortex dynamics is a rearrangement, i.e. that the formal solution is given by

$$q(x, y, t) = q_0(x_0(x, y, t), y_0(x, y, t)),$$

where $x_0(x, y, t)$ and $y_0(x, y, t)$ represent the inverted solutions to the characteristic equations. Thus if one has an isolated single-signed patch of vorticity surrounded by zero vorticity, and one wants to minimize the energy of this patch subject to continuous rearrangement, then this can be accomplished by the spreading out of the patch concomitantly with the stretching of the patch boundary, in such a way as to interpenetrate regions of zero and patch vorticity (cf. Fig. 15). Thus although the constraint does not preclude the march to zero energy, it does enforce a manner in which it can take place. This is the mechanism of Kelvin's sponge. In Section 3 we will see how DSA-dynamics accomplishes this with the inclusion of additional constraints.

3. Vortex examples

In this section we consider a variety of examples. In Section 3.1 we explore the various dynamics of Section 2.5 for two-fold symmetric initial conditions with the vorticity being of single sign and, where applicable, the two-fold symmetric Dirac constraints of (1) and (25). In Section 3.2, three-fold symmetric evolution with single-signed vorticity is considered under DSA-dynamics. Finally, in Section 3.3 we consider evolution under dipole initial conditions.

For all the single-signed, i.e. monopolar, runs the unit of time is determined by the value of the integrated vorticity. For example, this tends to be around π for the monopolar runs, giving a particle circulation time of about 4π. A Kirchhoff ellipse with an aspect

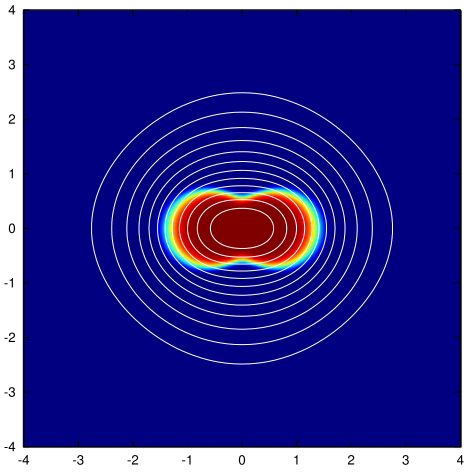

Fig. 2. The initial condition of (42). This vorticity (shading) and corresponding streamfunction (contours) is used for the runs of Figs. 3–18.

ratio 2 to 1 rotates at $\Omega = 2/(2+1)^2 = 2/9$, giving a period of about 28.3. The runs lasting until $t = 200$, then, represent about 16 revolutions of the particles and 7 of the ellipses.

All runs were done at a resolution of 256×256 points with a total domain size of 8 or 16 units with the scale of the initial condition being on the order of one unit. A pseudospectral code was used with integrals evaluated as sums and time advancement accomplished by second order Adams–Bashforth.

To give some insight into the ways energy and angular momentum change as a vortex shapes change, we have plotted H–L diagrams for several vortex structures: the Kirchhoff elliptical vortex, a "coarse-grained" circular vortex with a larger radius but smaller value of q ($q = a^{-2}$ for $r < a$), and cases in which some of the vorticity has been spread into an annular band around a smaller core ($q = 1$ for $r < b$ and $(1-b^2)/(a^2-b^2)$ for $b < r < a$). Fig. 1 shows the energy-angular momentum relationships as parametric curves with aspect ratio or a varying along the curves. The maximum H and L occur for all cases when the vortex is circular with unit radius and $q = 1$, corresponding to the aspect ratio or a being unity. For reference, we have marked with a circle the well-known stability threshold on the ellipse curve, where the aspect ratio is equal to three. Ellipses below this mark are linearly unstable. We will find it convenient to interpret some of our results in terms of this figure.

3.1. Single-signed vorticity with two-fold symmetry

For most of the runs of this subsection we use an initial condition of the following form:

$$q = \mathrm{e}^{-(r/r_0)^{10}} \quad \text{with } r_0 = 1 + \epsilon\cos(2\theta), \tag{42}$$

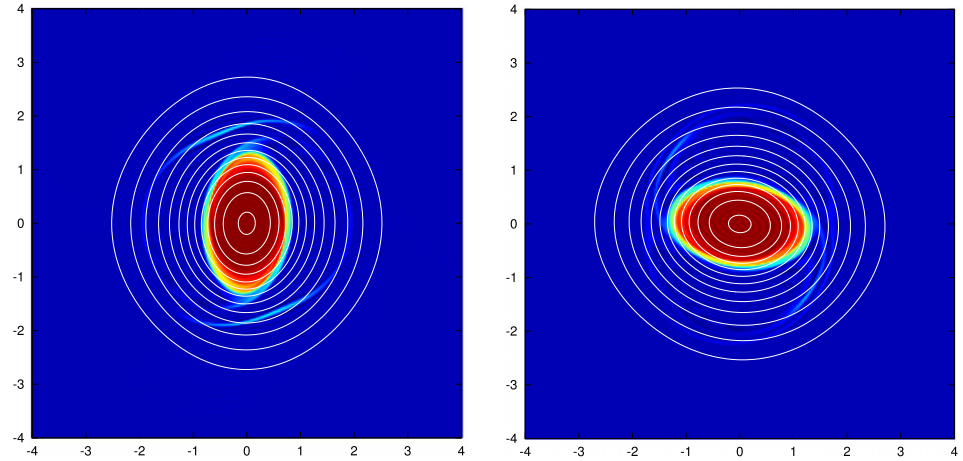

(a) $t = 40$. (b) $t = 80$.

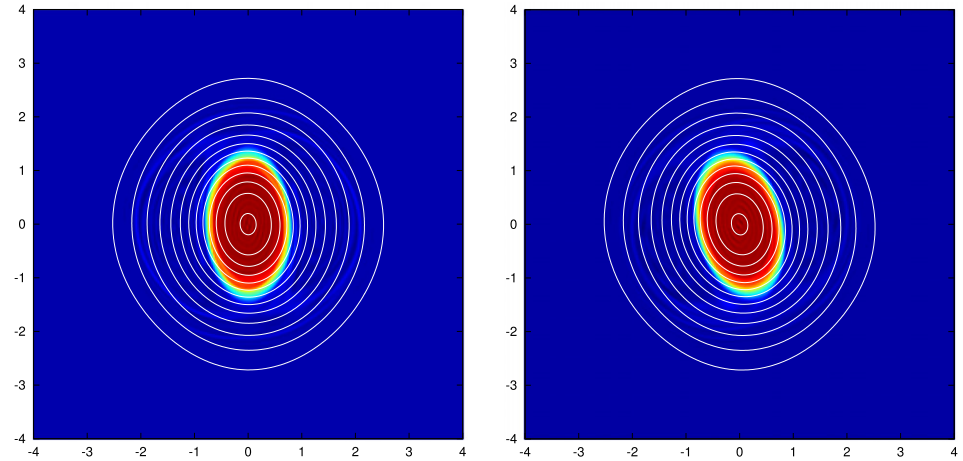

(c) $t = 120$. (d) $t = 200$.

Fig. 3. Vorticity (shading) and streamfunction (contours) under the H-dynamics of (37) with the two-fold symmetric initial condition of (42) at the times shown.

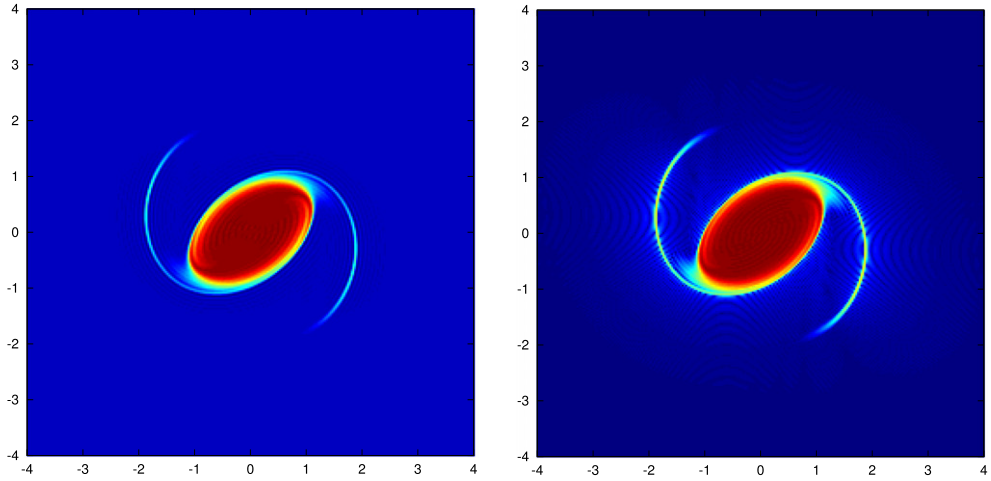

(a) q. (b) $\sqrt{q}$.

Fig. 4. Depiction of filaments forming under the H-dynamics of (37) with the same parameters and initial condition as those of Fig. 3. The snapshot is at $t = 20$. Panel (a) is the vorticity q, while (b) is $\sqrt{q}$ in order to accentuate the filaments.

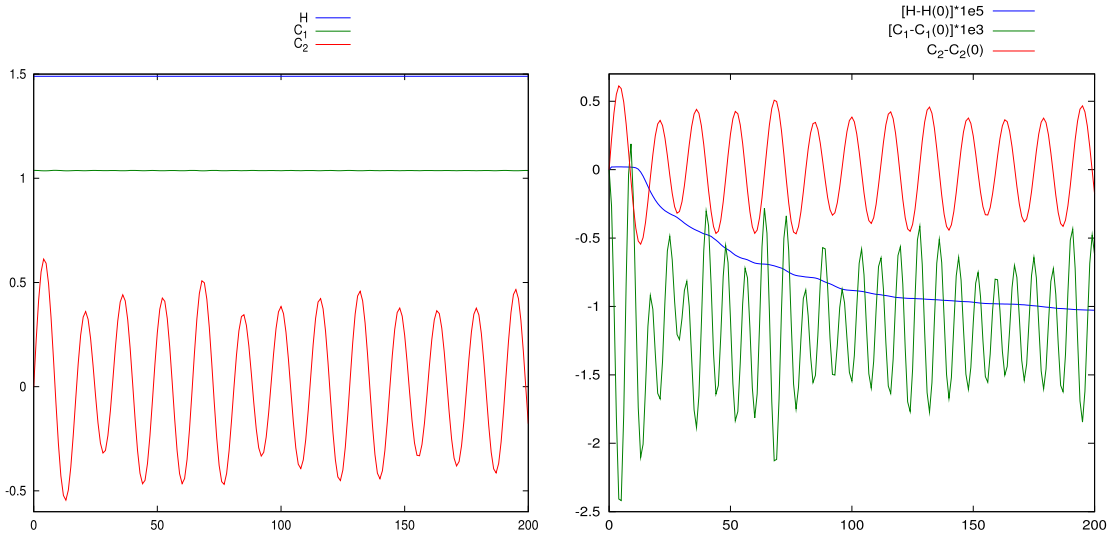

(a) H and $C_{1,2}$. (b) $H - H(0)$ and $C_{1,2} - C_{1,2}(0)$.

Fig. 5. Evolution (a) and relative evolution (b) of the Hamiltonian and the quantities $C_1 = -L$ of (1) and $C_2 = S$ of (25), under the pure H-dynamics of (37) for the initial condition of Fig. 2. Note, for clarity in panel (b) $H - H(0)$ has been amplified by 10^5 and $C_1 - C_1(0)$ by 10^3.

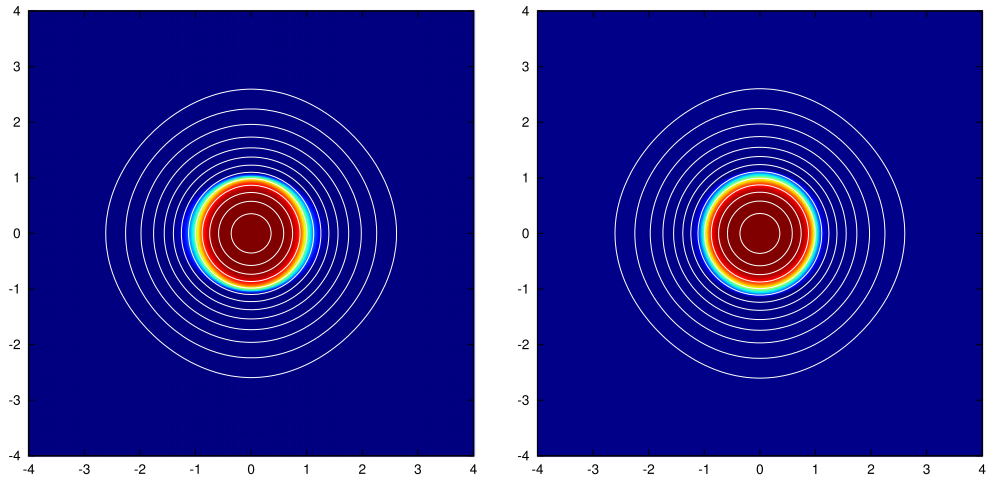

(a) $t = 20$. (b) $t = 100$.

Fig. 6. Vorticity (shading) and streamfunction (contours) under the pure ($\sigma = 0$) SA-dynamics of (39) with the two-fold symmetric initial condition of (42) for the times shown. The parameter $\alpha = 1$. The code maximizes energy while preserving the Casimir invariants (rearrangement of vorticity) arriving at the circular state.

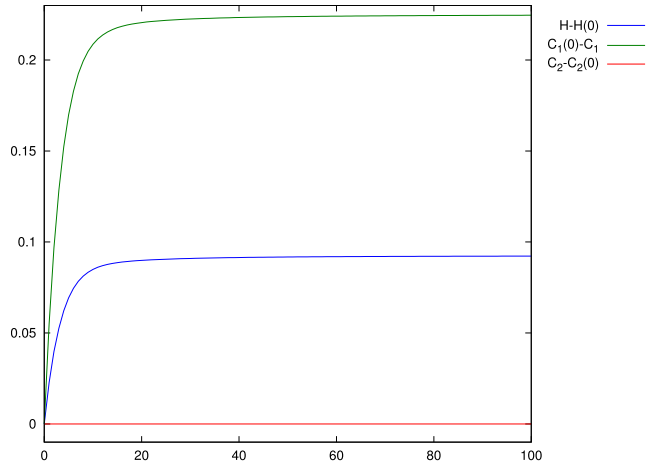

Fig. 7. Plots of the Hamiltonian, H, the angular momentum, $L = -C_1$, and the strain moment, $C_2 = S$, (relative to their initial values) vs. time, corresponding to Fig. 6, for the pure SA-dynamics of (39). The energy H approaches a maximum, while the angular momentum increases.

where $r = \sqrt{x^2 + y^2}$ and $\theta = \tan^{-1}(y/x)$. We choose $\epsilon = 0.4$ for all such runs. This initial condition is depicted in Fig. 2. Also, when Dirac constraints are used, we will take $C_1 = -L$, where the angular momentum L is defined in (1) and $C_2 = S$, the strain moment defined by (25). With these choices for the constraints and initial condition, we expect the system to evolve toward a state with two-fold symmetry.

Fig. 3 shows the vorticity and contours of the streamfunction for the H-dynamics of (37). Observe that the system sheds filaments, evolves toward an elliptical vortex state close to the Kirchhoff vortex in a time $t \gtrsim 20$, and then rotates uniformly for a long period of time. Fig. 4 shows an example of filament shedding at an early time. However, Fig. 5 shows that the invariants H and $C_1 = -L$ are well-conserved, as seen in Fig. 5(b), but H decreases monotonically at a small rate and C_1 has an oscillatory behavior that is likely due to the fact that the 2-torus is nonaxisymmetric. The strain moment $C_2 = S$ is not an invariant of H-dynamics, and this is evident from the figure. The vortex may continue to axisymmetrize slowly as vorticity is lost into filaments and spread around the core; in terms of the H–L diagram of Fig. 1, this would correspond to numerical dissipation decreasing H while preserving L, going from the ellipse towards an annular state.

Fig. 6 shows evolution with the same initial condition but now under the pure SA-dynamics of (39), i.e. with $\sigma = 0$ and $\alpha = 1$. In a fairly short time, $t \approx 20$, the system forms a long-lived axisymmetric vortex state. For SA-dynamics the Hamiltonian should be maximized at fixed Casimir invariants, as described in Section 2.5, but there is no reason the angular momentum should be conserved. Indeed, in Fig. 7 it is seen that the system reaches the axisymmetric vortex state as the energy grows to a

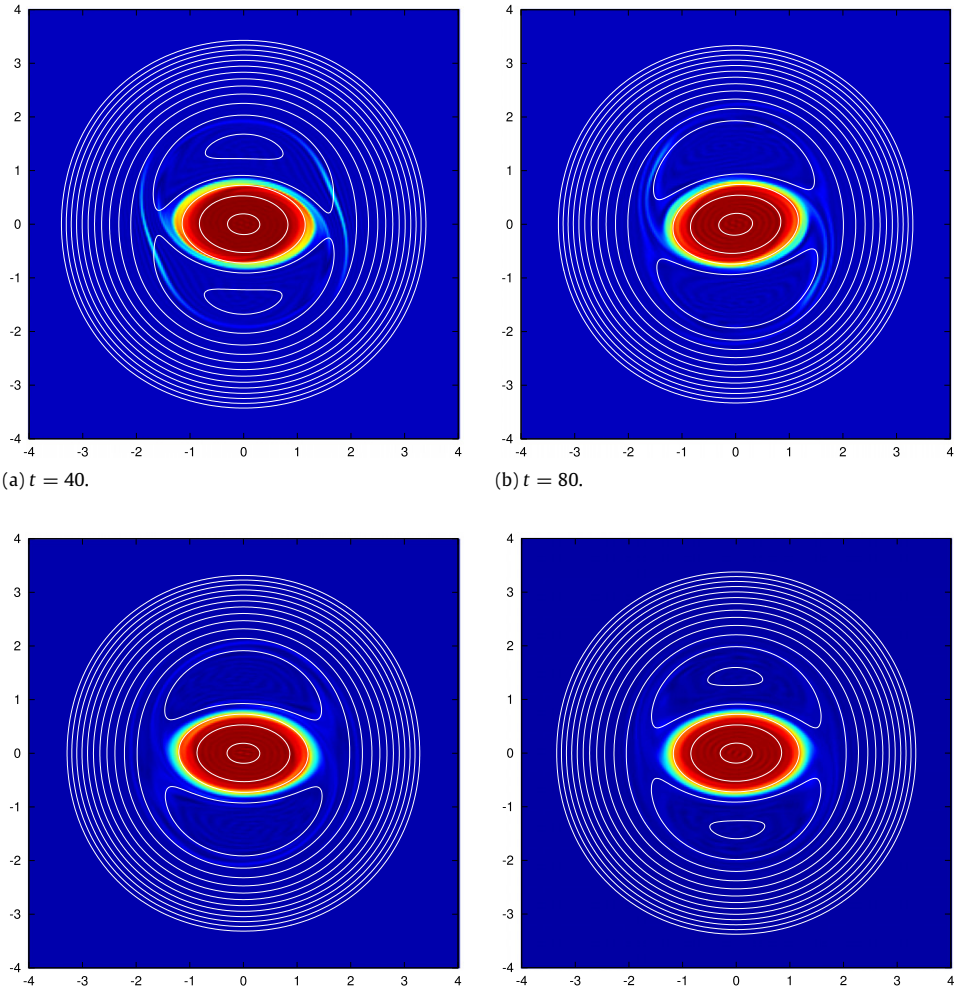

(a) $t = 40$. (b) $t = 80$.

(c) $t = 120$. (d) $t = 200$.

Fig. 8. Vorticity (shading) and streamfunction (contours) under the HD-dynamics of (38) with the two-fold symmetric initial condition of (42) for the times shown. The Dirac constraints C_1 and C_2, minus the angular momentum and the strain moment, of (1) and (25), respectively, were used.

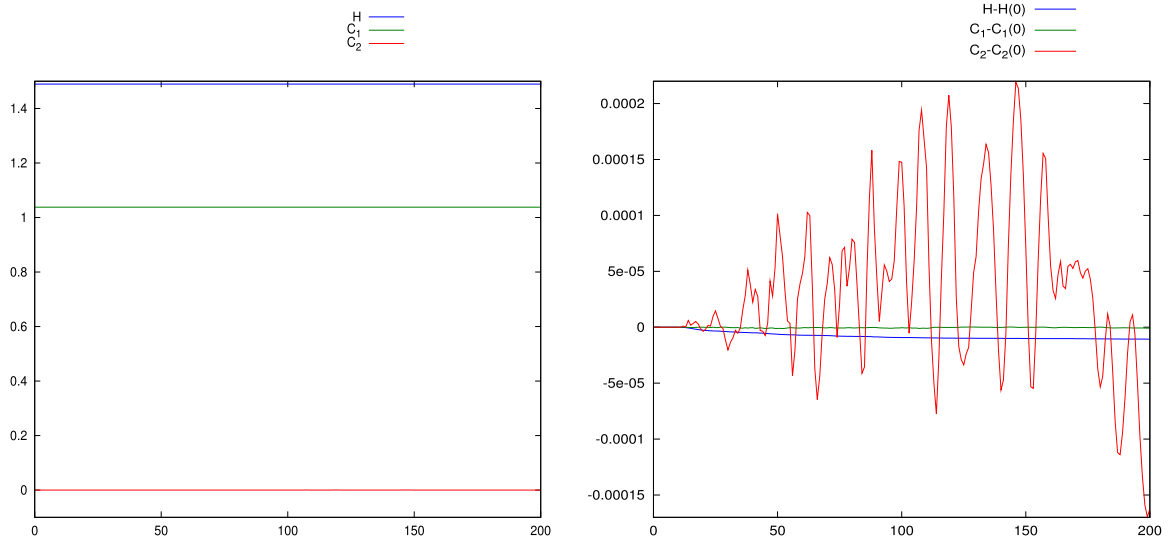

(a) H and $C_{1,2}$. (b) $H - H(0)$ and $C_{1,2} - C_{1,2}(0)$.

Fig. 9. Evolution (a) and relative evolution (b) of the Hamiltonian and the Dirac constraints $C_{1,2}$ vs. time, corresponding to the pure HD-dynamics of Fig. 8.

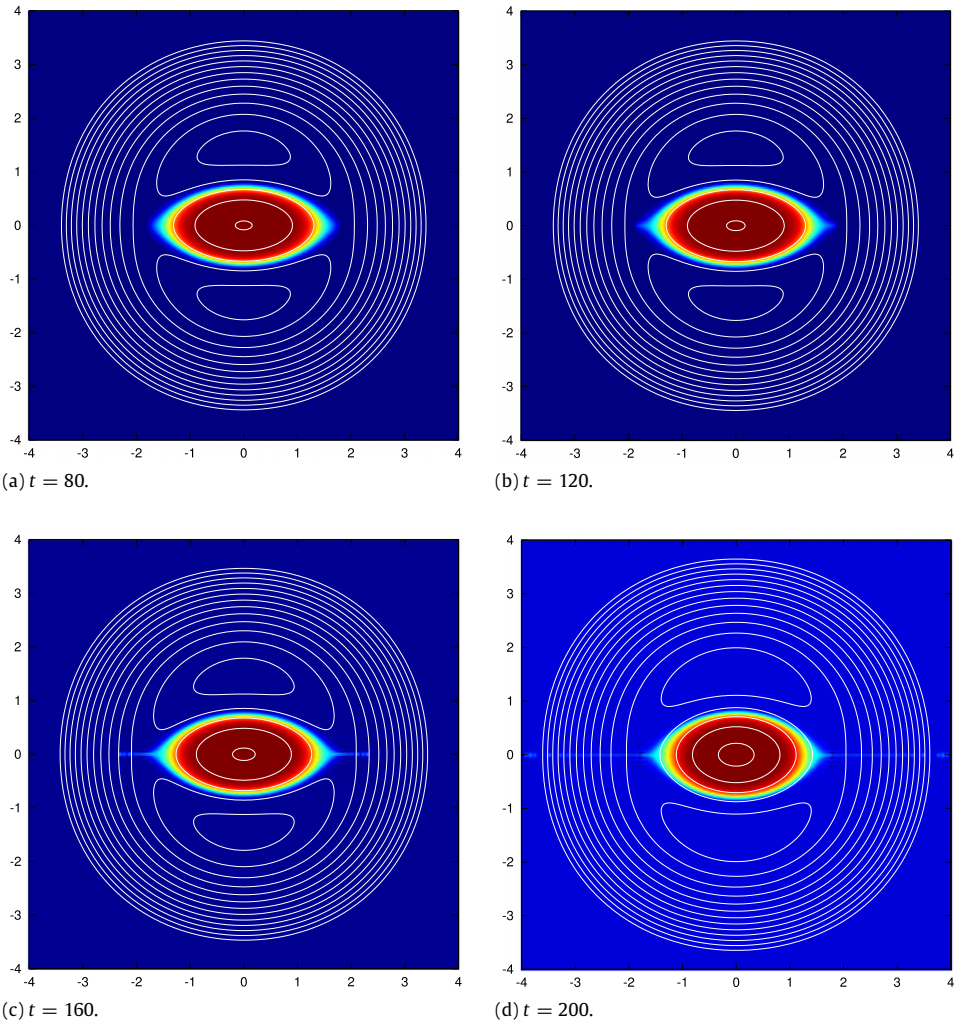

(a) $t = 80$. (b) $t = 120$.

(c) $t = 160$. (d) $t = 200$.

Fig. 10. Vorticity (shading) and streamfunction (contours) under the pure ($\sigma = 0$) DSA-dynamics of (40) with the two-fold symmetric initial condition of (42) for the times shown. The parameters $\sigma = 0$ and $\alpha = 1$; thus the bracket seeks to maximize the energy while striving to keep the C_1 and C_2 of (1) and (25) fixed. Observe for intermediate times q approaches a function of ψ, but for late times horizontal tines develop, and at later times yet the system begins to axisymmetrize. The lighter color of the background at $t = 200$ is due to the production of negative vorticity via numerical error.

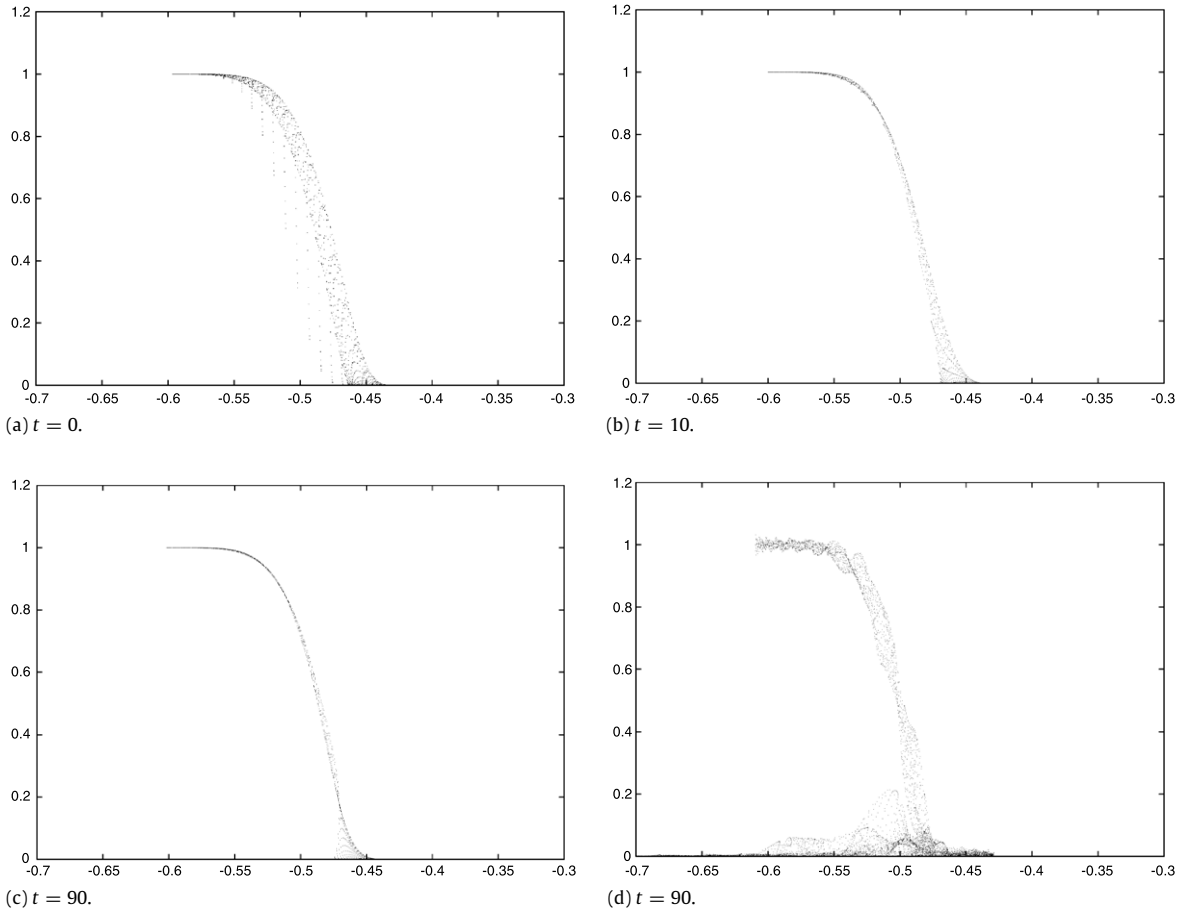

Fig. 11. Scatter plots of q vs. ψ for the DSA-dynamics of Fig. 10 are shown in panels (a)–(c) at the times indicated. For comparison, panel (d) shows a scatter plot for the HD-dynamics of Fig. 8 with the same initial condition.

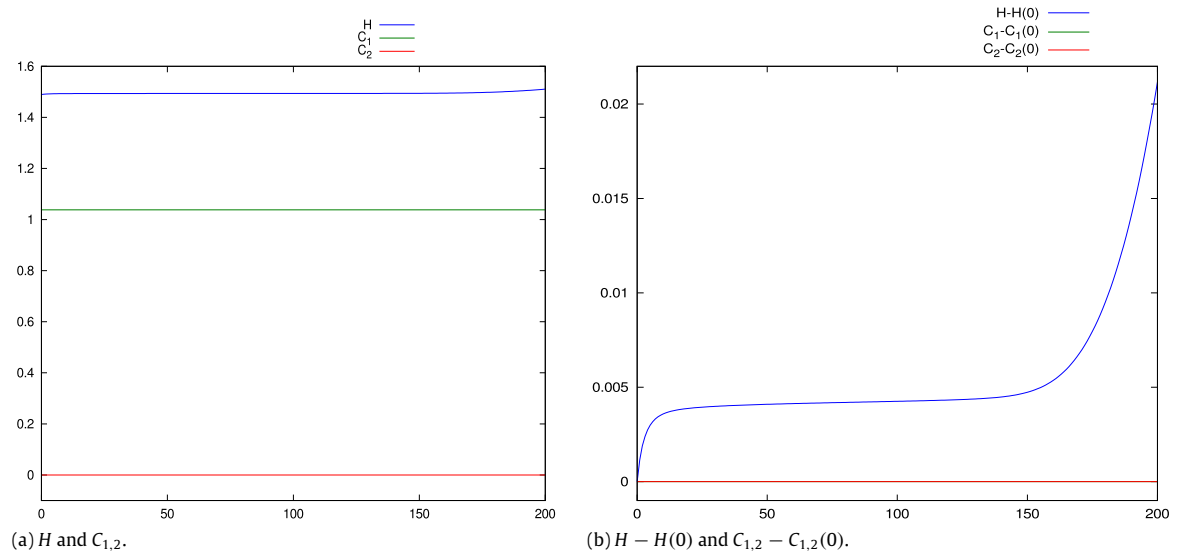

Fig. 12. Evolution (a) and relative evolution (b) of the Hamiltonian and the Dirac constraints $C_{1,2}$ vs. time, corresponding to the pure DSA-dynamics of Fig. 10. The late time rise in H signals the formation of tines and an approach to axisymmetry.

maximum value, and during this period the angular momentum $(-C_1)$ steadily increases. The quantity C_2 nearly vanishes initially and remains small because of symmetry. Note that choosing $\sigma = 0$ means that the system cannot homogenize the Casimir invariants with the H-dynamics, which could speed up the process, but must rely entirely on the symmetric bracket. If the numerics were exact this state would correspond to the energy maximum consistent with vorticity rearrangement. Similar axisymmetric vortex states were obtained by this method in [13,14]. Given the freedom to move in the H–L diagram, the system can maximize both H and L by moving towards the upper right on Fig. 1.

Fig. 8 shows the result for the pure HD-dynamics of (38) with C_1 again chosen to be minus the angular momentum and C_2 the straining moment, as given in (25). Observe that the

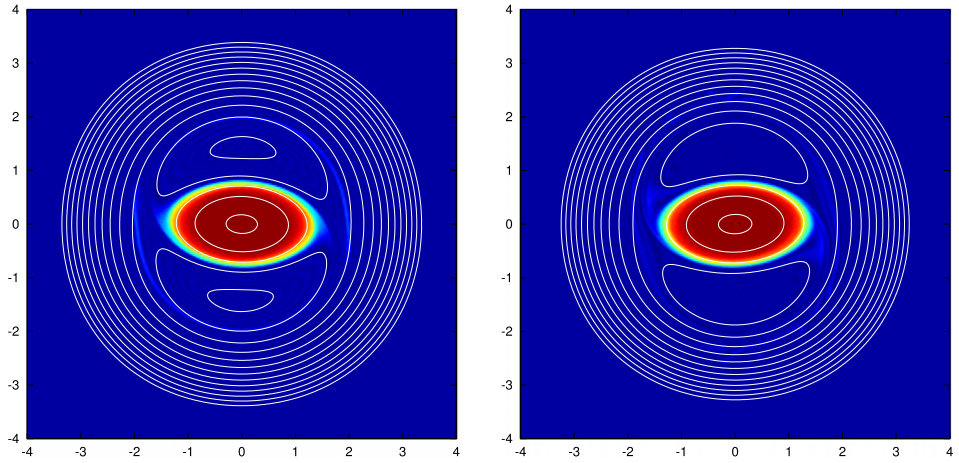

(a) $t = 40$. (b) $t = 80$.

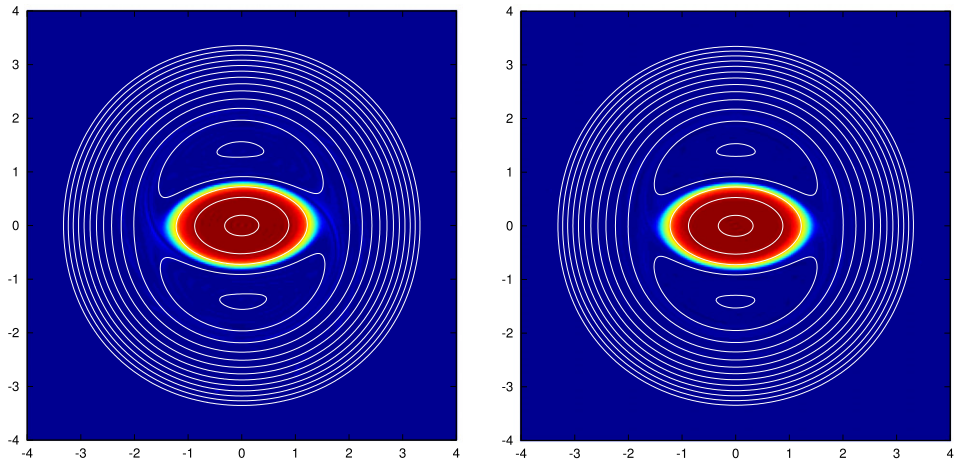

(c) $t = 120$. (d) $t = 200$.

Fig. 13. Vorticity (shading) and streamfunction (contours) under the DSA-dynamics of (40) with the two-fold symmetric initial condition of (42) for the times shown. The parameters $\alpha = 1$ and $\sigma = 1$. The code strives to maximize the energy while keeping C_1 and C_2 of (1) and (25) fixed. Setting $\sigma = 1$ gives more freedom to rearrange, and the tines of Fig. 10 no longer appear.

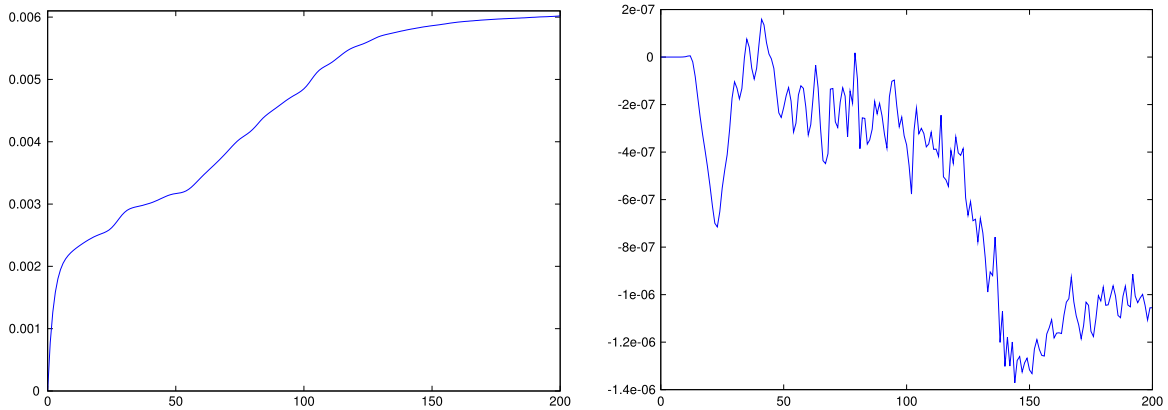

(a) $H/H(0) - 1$. (b) $C_1/C_1(0) - 1$.

Fig. 14. Evolution of (a) the relative Hamiltonian and (b) the Dirac constraint $C_1 = -L$ under DSA-dynamics with $\sigma = 1$, corresponding to the run of Fig. 13 without tines.

system relaxes to a state reminiscent of the Kirchhoff vortex, but unlike the case for H-dynamics it does not rotate. Also, unlike the results for SA-dynamics of Fig. 6 the system is constrained away from achieving the axisymmetric state, the absolute maximum consistent with constancy of the Casimir invariants. One does not expect asymptotic stability in this dynamics, but the formation of small scale structures by the shedding of filaments foments this process. In Fig. 9 the three invariants are seen to be well-conserved.

In Fig. 10 the initial condition of Fig. 2 is evolved under the DSA-dynamics of (40) with $C_1 = -L$ and $C_2 = S$ defined by (1)

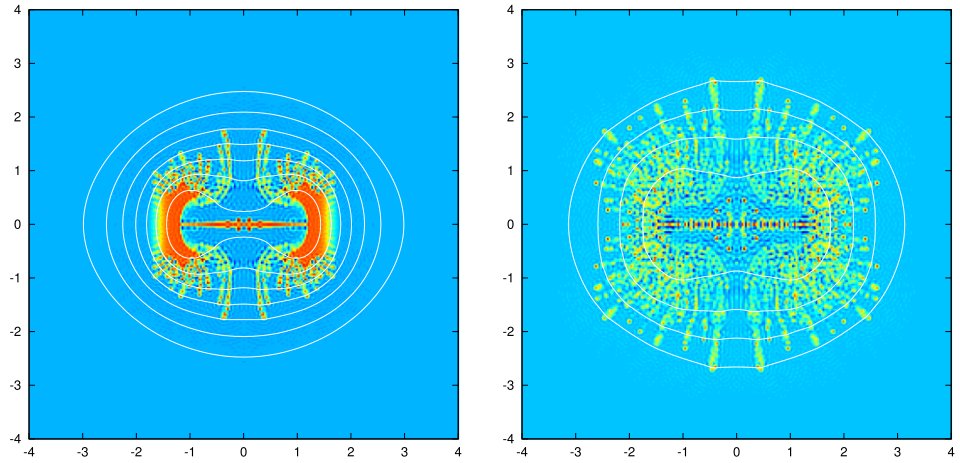

(a) $t = 20$. (b) $t = 40$.

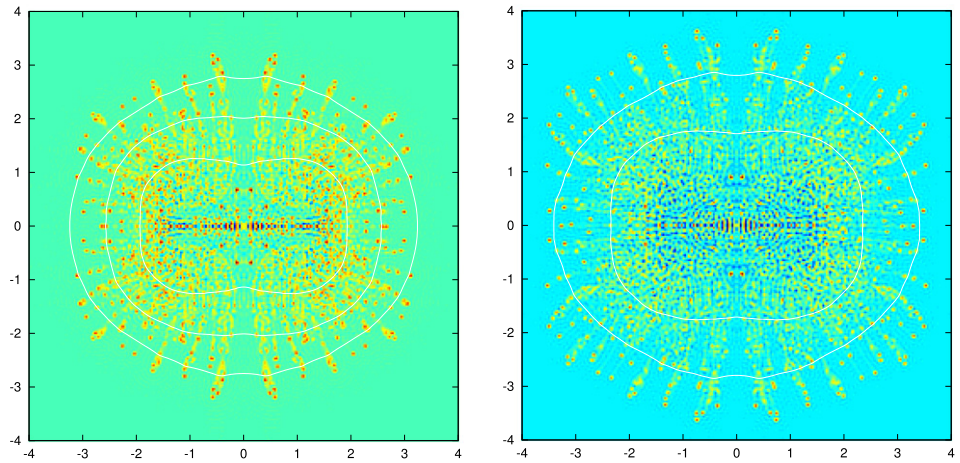

(c) $t = 60$. (d) $t = 100$.

Fig. 15. Vorticity (shading) and streamfunction (contours) under the SA-dynamics of (39) with the two-fold symmetric initial condition of (42) for the times shown. Here $\alpha = -1$ and $\sigma = 0$. The code seeks to minimize energy subject to the constancy of the Casimir invariants, and produces an expanding sponge-like state of interpenetrated regions of vorticity.

and (25), respectively. The parameters $\alpha = 1$ and $\sigma = 0$. As was the case for the runs of Fig. 6, $\sigma = 0$ means that the system cannot homogenize the Casimir invariants with the H-dynamics, which could speed up the process, but must rely entirely in this case on the dynamics of the symmetric bracket built from the Dirac bracket. Nevertheless, comparison of the contours with the shading in Fig. 10 indicates that q is approaching a function of ψ. This is further evidenced in Fig. 11 where it is shown more explicitly how q approaches a function of ψ. In this figure we also show a scatter plot for the HD-dynamics of Fig. 8 at the same time $t = 90$. However, at later times it is evident that the system is not constrained enough, because horizontal tines develop and eventually the method breaks down, as evidenced by the incipient breakdown of the near exact conservation of $C_1 = -L$ and H as seen in Fig. 12. At around $t = 100$ the energy makes a precipitous rise that signals a transition to a more axisymmetric state. This dynamics should be a rearrangement which preserves maximum and minimum values of q. However, note that some numerical error is present since $\min(q) = -0.0969$, which in light of (42) should be zero, but $\max(q) = 1.0001$ is preserved very well.

In Fig. 13 the initial condition of Fig. 2 is again evolved under (40) with the same Dirac constraints of (1) and (25), but with the parameters $\alpha = 1$ and $\sigma = 1$. Choosing $\sigma = 1$ means that the HD-dynamics contributes and it can homogenize while maintaining the Casimir invariant constraints and possibly cause

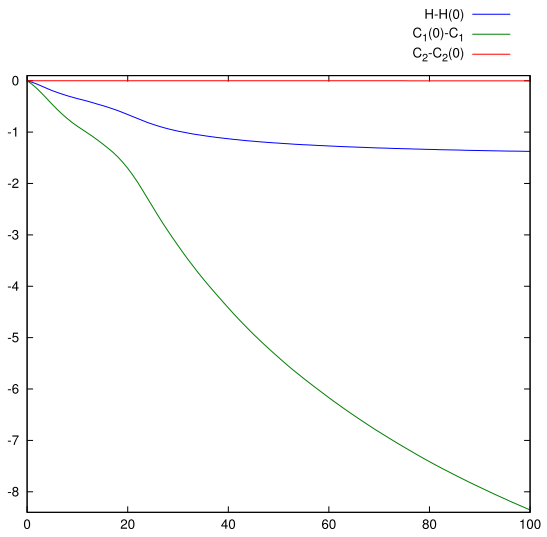

Fig. 16. Plots of the relative Hamiltonian H and $C_{1,2}$ vs. time for the run of Fig. 15, which is SA-dynamics with $\alpha = -1$ and $\sigma = 0$. Observe that H is decreasing in a manner expected by the production of the sponge-like state, but angular momentum decreases as the pattern spreads out. The quantity $C_2 = S$, the strain moment of (25), remains relatively flat.

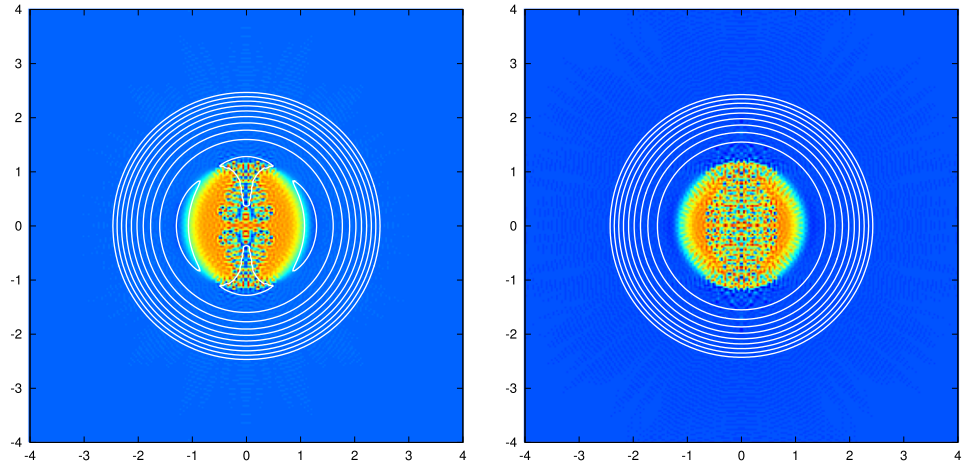

(a) $t = 20$. (b) $t = 40$.

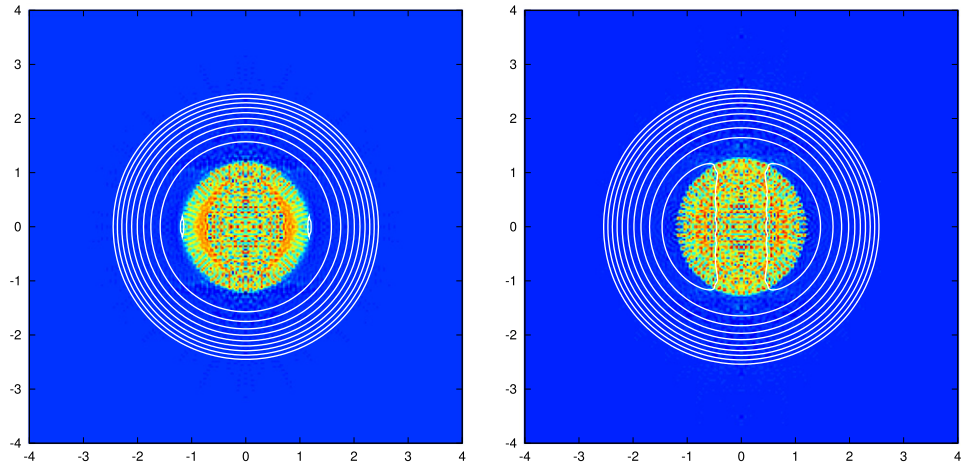

(c) $t = 60$. (d) $t = 100$.

Fig. 17. Vorticity (shading) and streamfunction (contours) under the DSA-dynamics of (40) with the two-fold symmetric initial condition of (42) for the times shown. Here $\alpha = -1$ and $\sigma = 0$. As in Fig. 15 the code seeks to minimize energy at fixed Casimir invariants, and thereby produce a sponge-like structure. However, in this case because the angular momentum is conserved the spreading of the structure is inhibited.

a more stable relaxation. This is akin to the rapid homogenization along streamlines (cf. e.g. [27]). Observe in Fig. 13 that the tines no longer develop. Examination of Fig. 14 reveals that the Hamiltonian relaxes well, and, although $C_1 = -L$ jitters about, it is still well-conserved. The solutions appear to be similar to those obtained in [28]. In terms of the H–L diagram of Fig. 1, these solutions correspond to motion vertically upward at fixed L until the elliptical state is reached, followed by a further vertical transition by throwing off filaments and arriving at something more like the annular states.

In the next two runs $\sigma = 0$, but the sign of α is flipped, i.e. $\alpha = -1$. This causes both the SA-dynamics and the DSA-dynamics to attempt to minimize the energy, and we expect something like the Kelvin sponge discussed in Section 2.6 to develop. In Fig. 15 we plot the case of pure SA-dynamics. Observe that regions of high and low vorticity interpenetrate and the entire structure spreads out in time. In Fig. 16 we see that energy is decreasing and that angular momentum decreases as the pattern spreads. This is consistent with the sponge results of [13,14].

In Fig. 17 we depict the situation under DSA-dynamics. Again a sponge-like pattern is produced, but because of the Dirac constraint C_1 the pattern cannot spread. Conservation of angular momentum inhibits the spreading, while conservation of the Casimir invariants induces the production of interpenetrating regions of

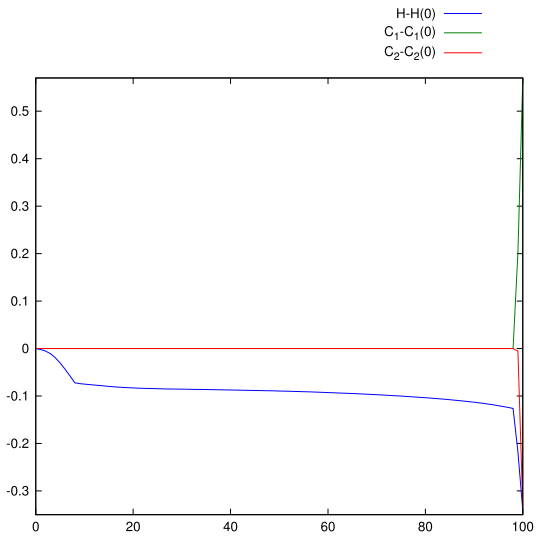

Fig. 18. Plots of the relative Hamiltonian and invariants $C_{1,2}$ vs. time for DSA-dynamics of Fig. 17, which has $\alpha = -1$ and $\sigma = 0$. Observe that energy is decreasing, first rapidly then steadily, at nearly constant angular momentum $L = -C_1$ and nearly constant strain moment $S = C_2$, consistent with a bounded sponge-like pattern.

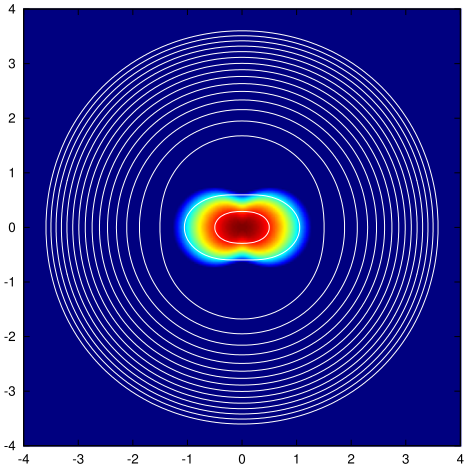

Fig. 19. The less sharp initial condition of (43) with $\epsilon = 0.6$ used for Fig. 20.

vorticity. The behavior of the energy and $C_{1,2}$ for this run are depicted in Fig. 18. Essentially a larger circular vortex with a lower coarse-grained vorticity is produced—one with a smaller energy but a small enough L.

The minimizations of both Figs. 15 and 17 can be interpreted in terms of the H–L diagram of Fig. 1. Both correspond to downward motion in the diagram to a "coarse-grained" state: for DSA-dynamics, the descent would be fairly vertical at constant L, while for the SA-dynamics of Fig. 15 the descent would include motion towards the left as well.

To conclude the set of runs with two-fold symmetry, we consider a less sharp initial condition:

$$q = \begin{cases} 1 - \left(\dfrac{r}{r_0}\right)^2 & r < r_0 \\ 0 & r > r_0 \end{cases} \quad \text{and} \quad r_0 = \sqrt{1 + \epsilon \cos(2\theta)} \tag{43}$$

with $\epsilon = 0.6$ and the square root in r_0 ensuring that the area within $r < r_0$ is π. This initial condition is depicted in Fig. 19. We again consider DSA-dynamics with the same constraints as above. Examination of Fig. 20 shows that the system finds a more gradual elliptical vortex state, and again the solutions appear to be similar to those in [28].

3.2. Single-signed vorticity with three-fold symmetry

Next we consider a three-fold symmetric initial condition of the form

$$q = \mathrm{e}^{-(r/r_0)^{10}} \quad \text{with } r_0 = \sqrt{1 + \epsilon \cos(3\theta)}, \tag{44}$$

with $\epsilon = 0.4$. In addition, the center ($r = 0$) of the vorticity above is shifted one grid point to the left ($x = -1/32$ in the units plotted)

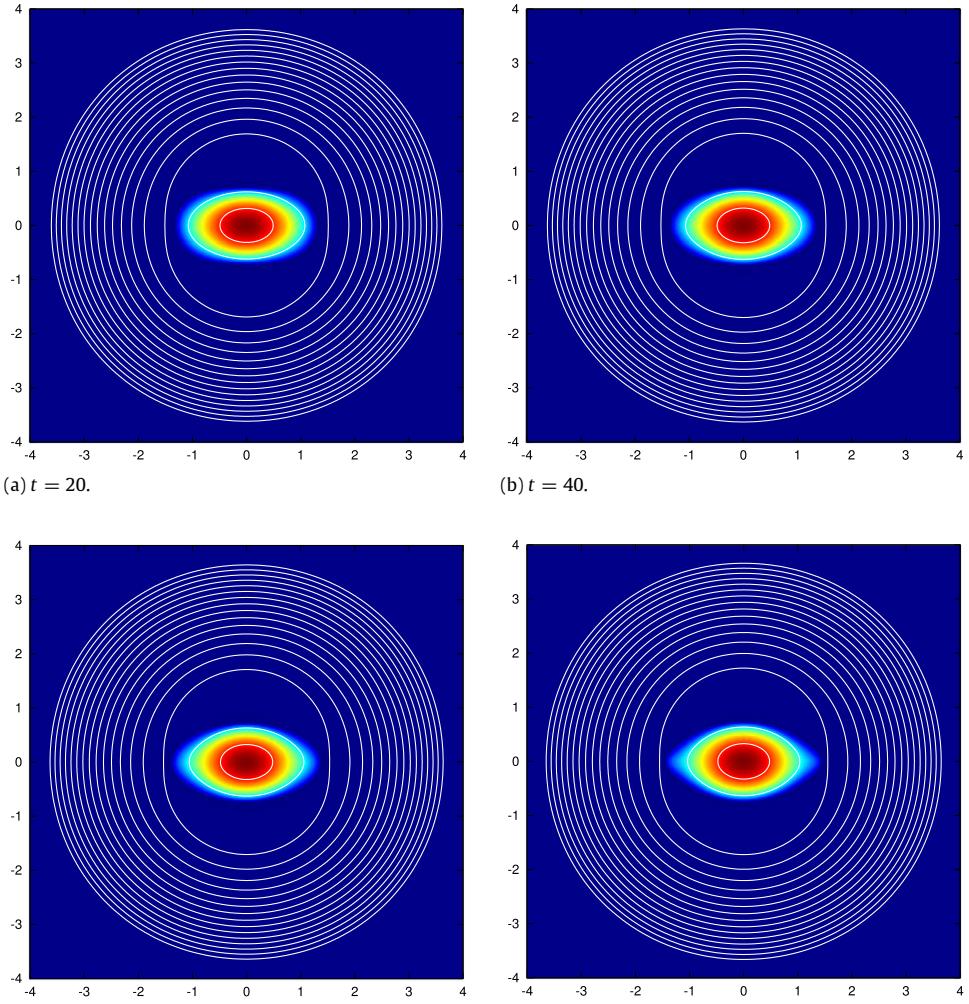

(a) $t = 20$. (b) $t = 40$.

(c) $t = 60$. (d) $t = 100$.

Fig. 20. Vorticity (shading) and streamfunction (contours) under the DSA-dynamics of (40) with the two-fold symmetric initial condition of (43) with $\epsilon = 0.6$, depicted in Fig. 19, for the times shown. Here $\alpha = 1$ and $\sigma = 0$.

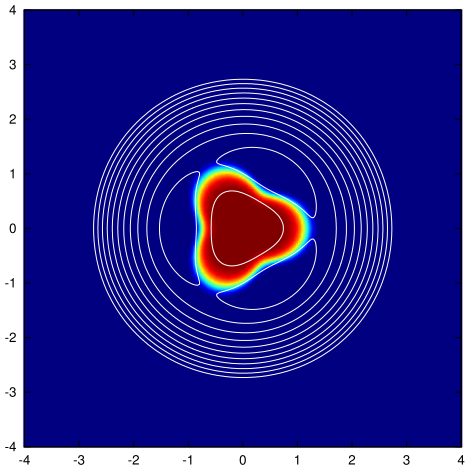

Fig. 21. The three-fold symmetric initial condition of (44) with $\epsilon = 0.4$, which is used for the runs of Figs. 22–25.

in order to put energy into an off-center perturbation. This initial condition is depicted in Fig. 21.

In this subsection, the Dirac constraint C_1 is still minus the angular momentum L of (1); however, C_2 will be taken to be the following cubic moment:

$$T = \int_{\mathcal{D}} \mathrm{d}\mathbf{x}\,(x^2 y - y^{3/3})q = \frac{1}{3}\int_{\mathcal{D}} \mathrm{d}\mathbf{x}\, r^3 \sin(3\theta)q, \tag{45}$$

which is chosen with the hope of enforcing three-fold symmetry.

Fig. 22 shows the evolution of (44) under DSA-dynamics with these two Dirac constraints, $C_1 = -L$ and $C_2 = T$, $\sigma = 0$, and $\alpha = 1$. As in other runs, the code seeks to maximize the energy at fixed Casimir invariants and Dirac constraints. Observe that a clear three-fold vortex state appears and remains until about $t = 40$ as the energy gradually increases, as depicted in Fig. 23. This state is reminiscent of the three-fold symmetric V-state of contour dynamics [29]. However, as time progresses three tines develop and eventually the code seeks a more axisymmetric state at higher energy. This latter stage is accompanied by a shift of the vortex that can be measured by the x-component of the 'center-of-q' defined by

$$\bar{x} := \frac{\int_{\mathcal{D}} \mathrm{d}\mathbf{x}\, x\, q}{\int_{\mathcal{D}} \mathrm{d}\mathbf{x}\, q}. \tag{46}$$

Observe in Fig. 23 that the axisymmetrization occurs in concert with a shift of $\bar{x}$ to the left. Although a centered axisymmetric vortex has a lower C_1 value, it can partially compensate by the excess associated with the displacement away from the origin. The

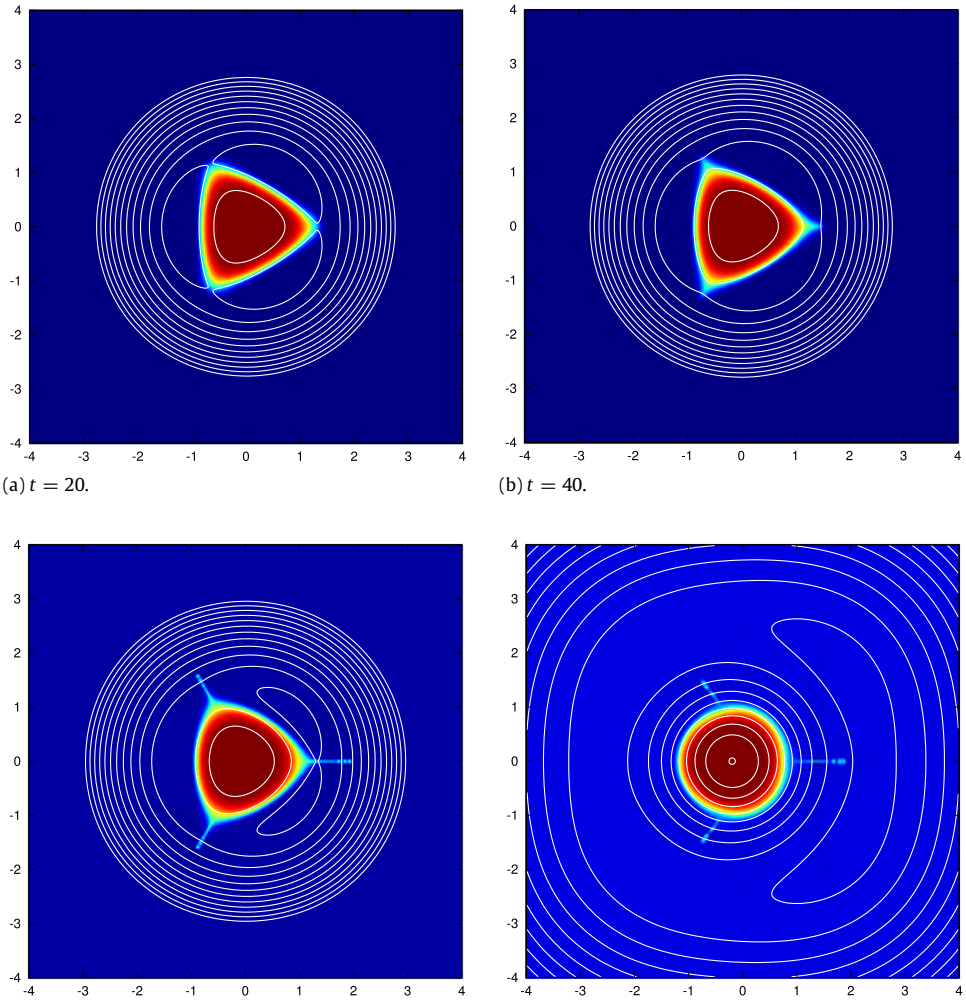

(a) $t = 20$. (b) $t = 40$. (c) $t = 60$. (d) $t = 80$.

Fig. 22. Vorticity (shading) and streamfunction (contours) under the DSA-dynamics of (40) with the three-fold symmetric initial condition of (44) with $\epsilon = 0.4$, depicted in Fig. 21, for the times shown. Here $\alpha = 1$ and $\sigma = 0$ and the Dirac constraints are $C_1 = -L$ of (1) and $C_2 = T$ of (45). For early times a three-fold symmetric vortex appears and remains until $t \approx 40$, then at later times there is a move to greater axisymmetrization with a shift of the vortex center to the left.

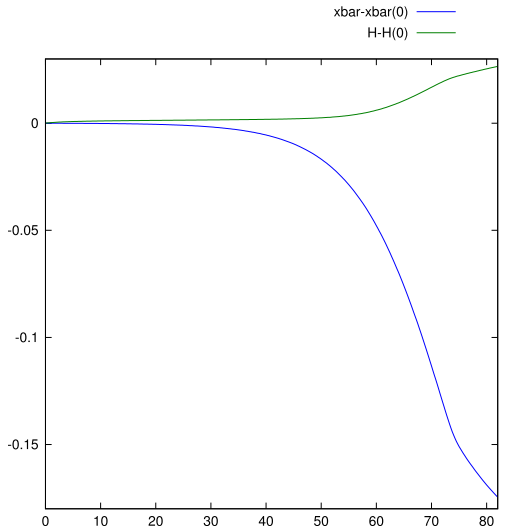

Fig. 23. Plots of the energy H and $\bar{x}$ defined by (46) under the DSA-dynamics corresponding to the run of Fig. 22. As in other runs, the code seeks to maximize the energy at fixed Casimir invariants and Dirac constraints, $C_1 = -L$ of (1) and $C_2 = T$ of (45). A three-fold vortex state appears early and remains for times up to $t \approx 40$, as the energy gradually increases. Subsequently, three tines develop and, coincident with decreasing $\bar{x}$ representing migration of the vortex center to the left, the code seeks a more axisymmetric state at higher energy—albeit one with angular momentum absorbed into the tines.

tines also appear to carry away some C_1 leaving this quantity fairly well conserved overall. The vortex is displaced along the zero line of the C_2 constraint, maintaining the value of this Dirac constraint as well. Thus, this appears to be a legitimate maximal H solution—one that has broken the three-fold symmetry.

Fig. 24 shows the evolution of (44) under DSA-dynamics with the same two Dirac constraints used for Fig. 22, viz. $C_1 = -L$, with L of (1) and $C_2 = T$, with T of (45), but now with $\sigma = 1$. As was the case for our two-fold symmetric runs, the tines no longer develop because the HD component homogenizes. Instead the angular momentum is taken up by an annular region around the central vortex.

Recall that the Dirac bracket of (16) can be constructed for any even number of constraints for which $\mathbb{C}$ exists. Thus, motivated by the results of Figs. 22 and 24, we seek to avoid axisymmetrization by adding additional constraints. To this end we consider the following two components of the linear momentum (deficit) as candidates for Dirac constraints:

$$P_y = \int_{\mathcal{D}} \mathrm{d}\mathbf{x}\, x\, q \quad \text{and} \quad P_x = -\int_{\mathcal{D}} \mathrm{d}\mathbf{x}\, y\, q. \tag{47}$$

If P_y were conserved, the shift in $\bar{x}$ would be prevented, since the denominator of $\bar{x}$, $\int_{\mathcal{D}} \mathrm{d}\mathbf{x}\, q$, is a Casimir invariant, and perhaps this could constrain the system away from axisymmetrization. Fig. 25 shows the results for DSA-dynamics with the four constraints, $C_{1,2}$ the same as the other runs of this section and $C_3 = P_y$ and $C_4 = P_x$.

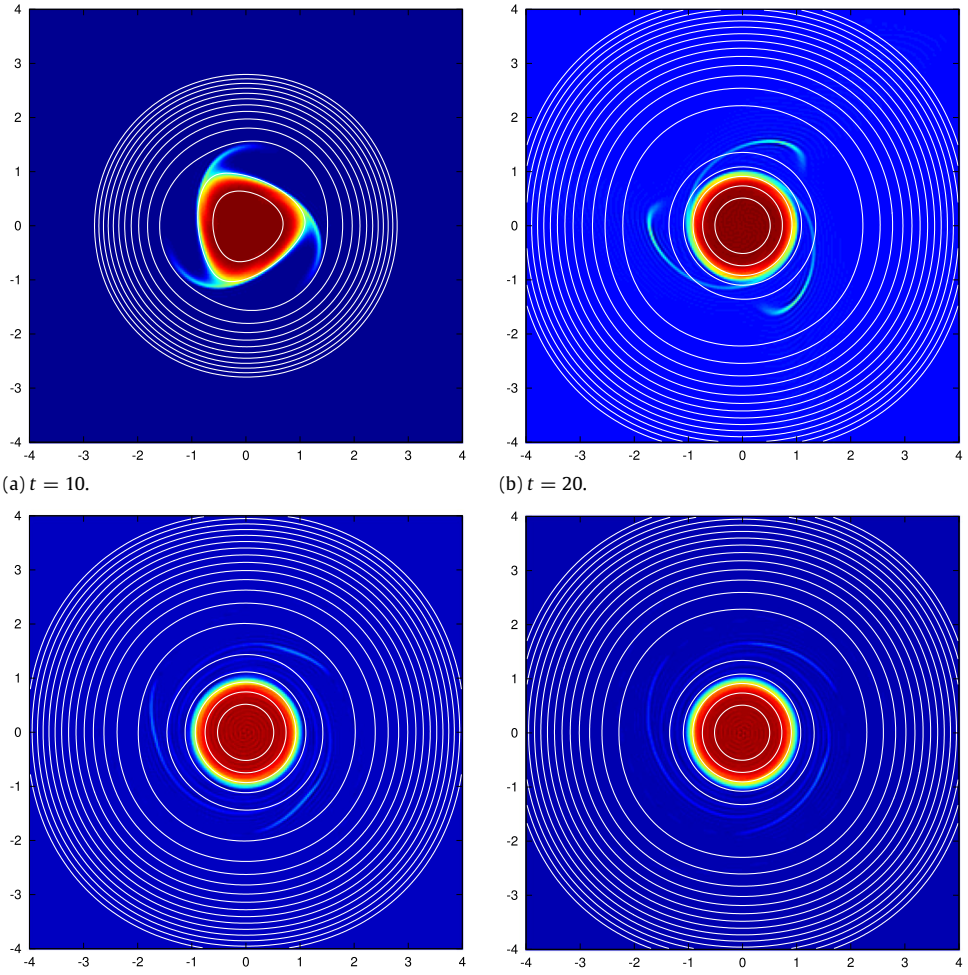

(a) $t = 10$. (b) $t = 20$. (c) $t = 40$. (d) $t = 50$.

Fig. 24. Vorticity (shading) and streamfunction (contours) under the DSA-dynamics of (40) with the three-fold symmetric initial condition of (44) with $\epsilon = 0.4$, depicted in Fig. 21, for the times shown. Here again the Dirac constraints are $C_1 = -L$ of (1) and $C_2 = T$ of (45) and $\alpha = 1$. However, now $\sigma = 1$. As in Fig. 22, at early times a three-fold symmetric vortex appears, but then at later times there is a move to greater axisymmetrization and the system rapidly finds the nearly axisymmetric state seen in (d). Instead of developing tines, the vorticity forms more of an outer annular ring.

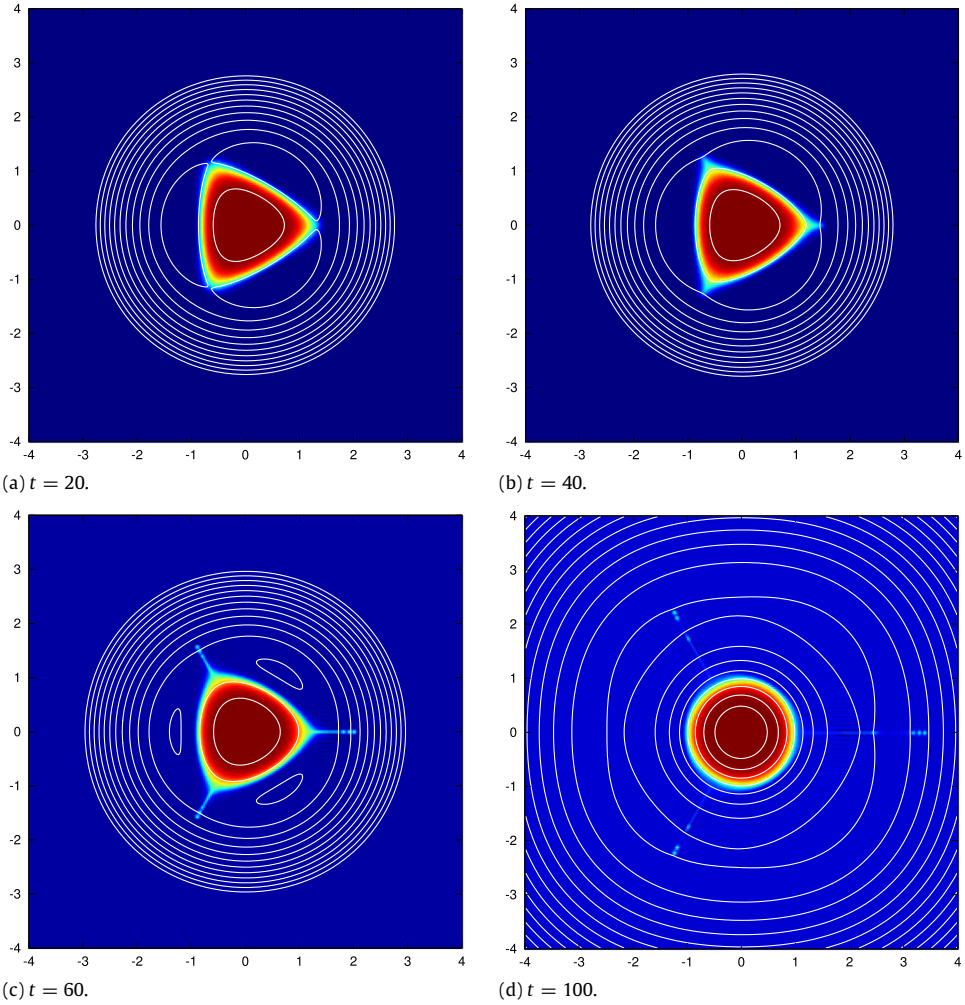

(a) $t = 20$. (b) $t = 40$.

(c) $t = 60$. (d) $t = 100$.

Fig. 25. Vorticity (shading) and streamfunction (contours) under the DSA-dynamics of (40) with the three-fold symmetric initial condition of (44) with $\epsilon = 0.4$, depicted in Fig. 21, for the times shown. Here $\alpha = 1$ and $\sigma = 0$ and four Dirac constraints are used: $C_1 = -L$ of (1), $C_2 = T$ of (45), $C_3 = P_y$ and $C_4 = P_x$ of (47). For early times a three-fold symmetric vortex appears and remains for a bit longer than the run of Fig. 22, $t \approx 50$, but again at later times there is a move to greater axisymmetrization accompanied by tines that take up the deficit in C_1.

We choose $\sigma = 0$ and use the same initial condition of (44). The code tracks the three-fold symmetric state for a bit longer, but eventually tends again to an axisymmetrized state with the presence of three tines. Observe in Fig. 26 that $\bar{x}$ remains fixed, indicating that the code respected its invariance, and the energy begins to rise steeply at around $t \approx 60$.

We suspect there are solutions with a nearly axisymmetric center surrounded by three small satellite vortices at the stagnation points. The latter could account for the deficit in C_1. When $\sigma = 1$, we may tend towards more of an annular ring.

3.3. Dipoles

Next we consider the dipole initial condition of the form

$$q = ye^{-r^2/2}, \tag{48}$$

which is depicted in Fig. 27. This form is reminiscent of the Lamb dipole vortex [30], but is clearly not the exact solution that involves Bessel functions.

The question of which constraints to use remains. Because dipoles translate, and, in particular, we expect the initial condition of Fig. 27 to translate to the right, we choose the x-component of the linear momentum, $P_x = C_1$ of (47), as one of our constraints. For the other we choose the strain moment $S = C_2$ of (25) used in Section 3.1.

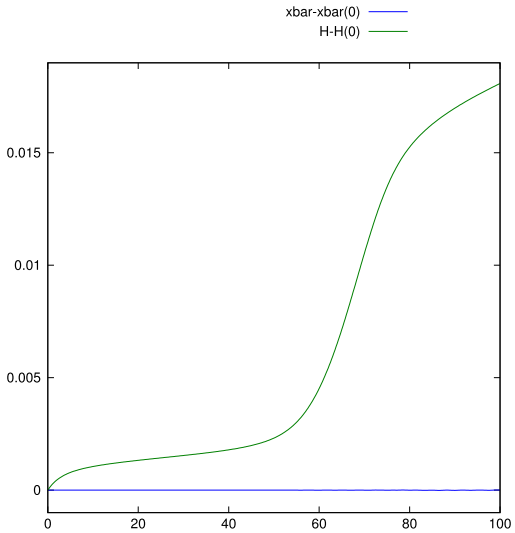

Fig. 26. Temporal evolution of the energy H and $\bar{x}$ defined by (46) under the DSA-dynamics corresponding to the run of Fig. 25. The code seeks to maximize the energy at fixed Casimir invariants and Dirac constraints, $C_1 = -L$ of (1), $C_2 = T$ of (45), $C_3 = P_y$, and $C_4 = P_x$ of (47). During the region of slower increase in H the system is near a three-fold symmetric state, but near $t \approx 50$ the energy increases rapidly and the code seeks a larger energy state of greater axisymmetry.

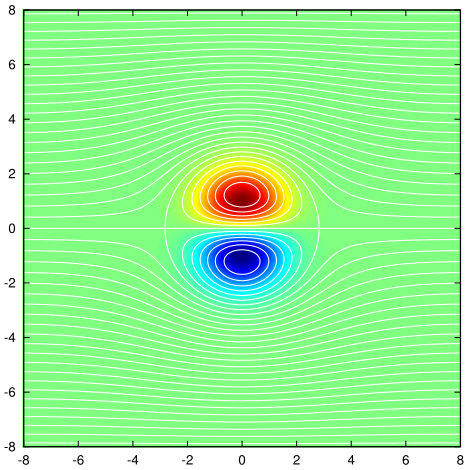

Fig. 27. The initial condition of (48), which is used for the run of Figs. 28 and 30.

Fig. 28 depicts the evolution of (48) under DSA-dynamics with $\sigma = 0$ and $\alpha = 1$. From Fig. 29 it is clear that the system seeks a higher energy state, that the Dirac constraints $C_{1,2}$ remain fixed to a good degree, and that a dipole structure remains. A closer look at $C_2 = S$ reveals trends because the doubly periodic boundary conditions assumed have some difficulty agreeing with the strain moment. If we run the same initial condition of (48) under SA-dynamics, the evolution behaves differently, as seen in Fig. 30 which depicts a late stage of this dynamics. Observe in this figure that the halves of the dipole are tending to separate, a behavior noted in [14] that is an avenue for increasing the energy. This separation is evident in Fig. 31, where $P_x = C_1$ is plotted. However, under our DSA-dynamics, enforcing P_x to be a Dirac constraint prevents the halves from separating in the y-direction. Thus, unlike SA-dynamics which strives to increase energy subject only to Casimir invariant conservation, our method is able to capture such dipole-like solutions.

4. Two-layer quasigeostrophy

Before presenting our two-layer numerical results in Section 4.2, we discuss the essentials of the Hamiltonian structure in Section 4.1 that are required for the calculations.

4.1. Two-layer Hamiltonian structure

The dynamics of the two layers is coupled through the Greens function matrix, defined by

$$\begin{pmatrix} \nabla^2 - h_2\gamma^2 & h_2\gamma^2 \\ h_1\gamma^2 & \nabla^2 - h_1\gamma^2 \end{pmatrix} \begin{pmatrix} \mathcal{G}_{11} & \mathcal{G}_{12} \\ \mathcal{G}_{21} & \mathcal{G}_{22} \end{pmatrix} = \begin{pmatrix} \delta(\mathbf{x}) & 0 \\ 0 & \delta(\mathbf{x}) \end{pmatrix}. \quad (49)$$

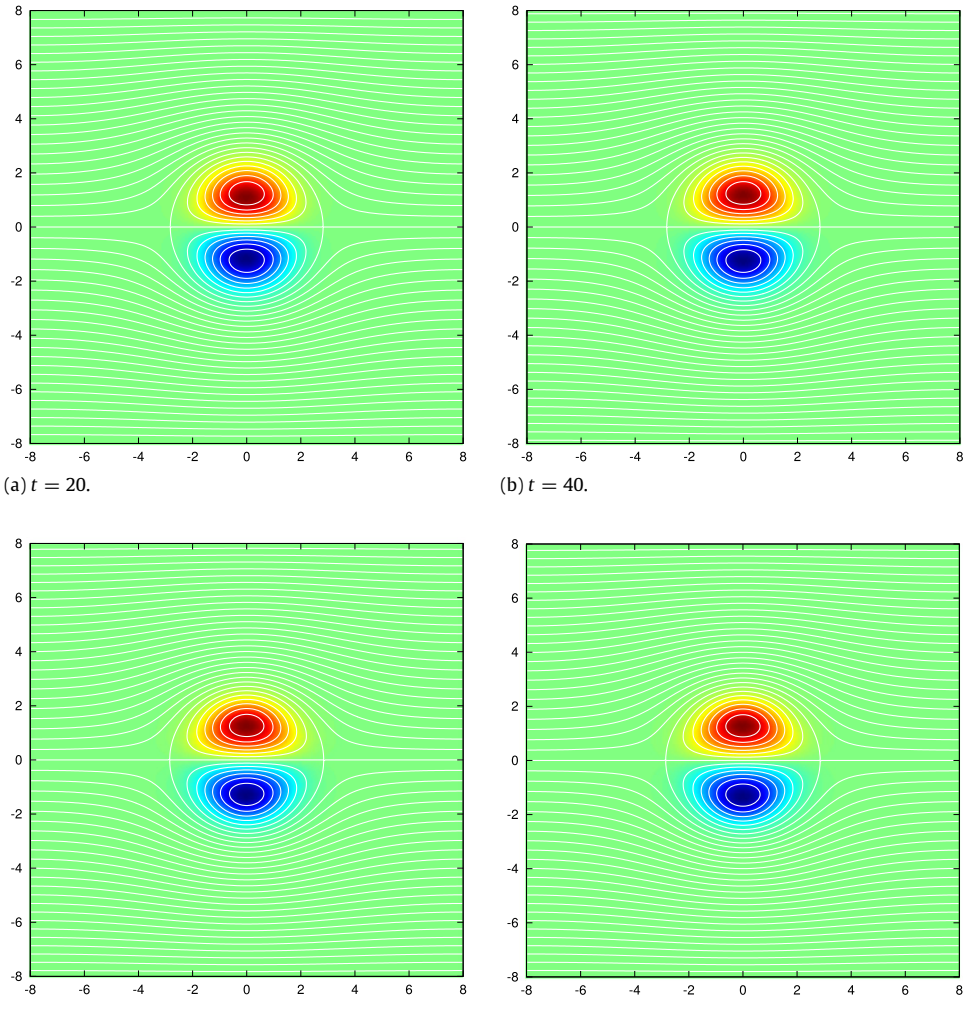

(a) $t = 20$. (b) $t = 40$.

(c) $t = 80$. (d) $t = 100$.

Fig. 28. Vorticity (shading) and streamfunction (contours) under the DSA-dynamics of (40) with $\sigma = 0$ and the dipole initial condition of (48) for the times shown. A stable dipole structure remains for long time without separation.

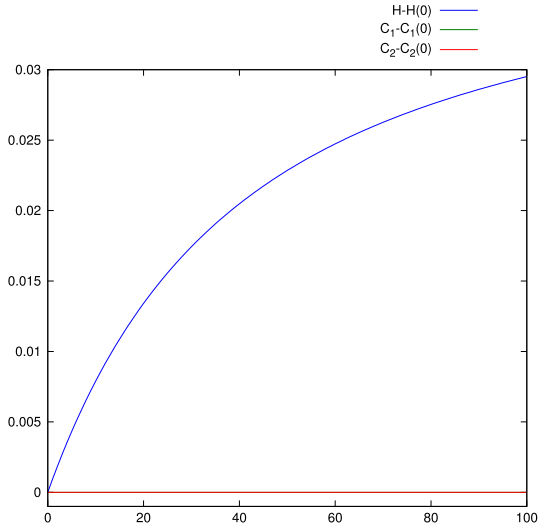

Fig. 29. Relative energy and Dirac constraints $C_1 = P_x$ and $C_2 = S$ vs. time for the initial condition of (48), which is used for the run of Fig. 28.

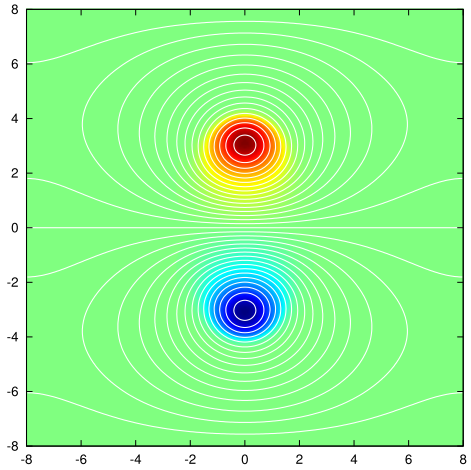

Fig. 30. The initial condition of (48), run to a time of $t = 200$ under SA-dynamics with $\alpha = 1$ and $\sigma = 0$. Observe, that without the P_x Dirac constraint the dipole has separated in the y-direction.

Here h_j is the fractional thickness of the jth layer and γ is the inverse of the deformation radius. A consequence of the form of (49) is the identity

$$h_j \mathcal{G}_{j1} = h_1 \mathcal{G}_{1j} \quad \text{(not summed)}, \tag{50}$$

which is trivial for $j = 1$ but not for $j = 2$.

The Hamiltonian of the system is given by

$$H = -\frac{1}{2} \sum_{i,j=1,2} \int_{\mathcal{D}} \mathrm{d}\mathbf{x} \int_{\mathcal{D}} \mathrm{d}\mathbf{x}'\, h_i\, q_i(\mathbf{x}) \mathcal{G}_{ij}(\mathbf{x}, \mathbf{x}') q_j(\mathbf{x}'), \tag{51}$$

which when substituted into the following Poisson bracket:

$$\{F, G\} = \sum_{i=1,2} \frac{1}{h_i} \int_{\mathcal{D}} \mathrm{d}\mathbf{x}\; q_i(\mathbf{x}) \left[\frac{\delta F}{\delta q_i(\mathbf{x})}, \frac{\delta G}{\delta q_i(\mathbf{x})} \right] \tag{52}$$

gives the two-layer equations of motion. To see this, note that

$$\frac{\delta H}{\delta q_1(\mathbf{x})} = -\frac{1}{2} \sum_{j=1,2} \int_{\mathcal{D}} \mathrm{d}\mathbf{x}'\, h_1 \mathcal{G}_{1j} q_j(\mathbf{x}') - \frac{1}{2} \sum_{j=1,2} \int_{\mathcal{D}} \mathrm{d}\mathbf{x}'\, h_j \mathcal{G}_{j1} q_j(\mathbf{x}'),$$

using the symmetry of $\mathcal{G}$ in $\mathbf{x}$ and $\mathbf{x}'$, and therefore with (50)

$$\frac{\delta H}{\delta q_1(\mathbf{x})} = -\int_{\mathcal{D}} \mathrm{d}\mathbf{x}'\, h_1 \mathcal{G}_{1j} q_j(\mathbf{x}') = -h_1 \psi_1(\mathbf{x}).$$

Consequently,

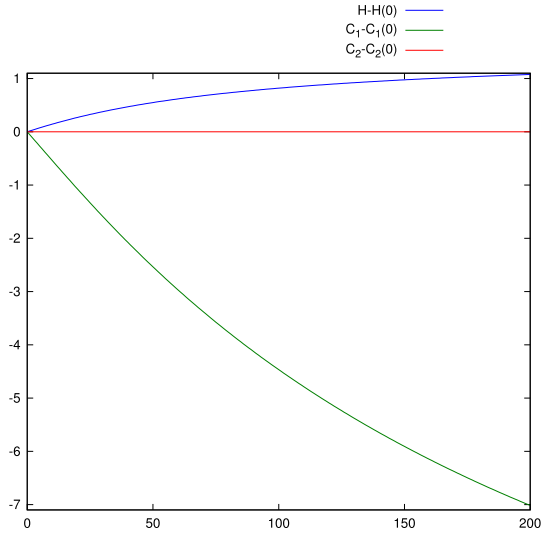

Fig. 31. Energy and quantities $C_1 = P_x$ of (47) and $C_2 = S$ of (25) vs. time for the initial condition of (48), under SA-dynamics corresponding to the run of Fig. 30. Note that the $C_{1,2}$, not being constrained are not conserved, although C_2 varies little. The steady decrease in C_1 corresponds to a steady increase in separation of the dipole in the y-direction.

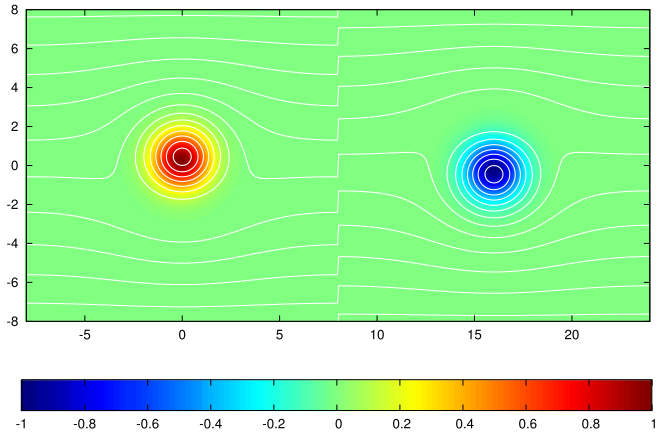

Fig. 32. The initial condition of (53), which is used for the run of Figs. 33 and 34. Layer-1 is the left panel with positive vorticity, while layer-2 is the right with negative vorticity.

$$\{q_1(\mathbf{x}), G\} = \left[\frac{1}{h_1} \frac{\delta G}{\delta q_1(\mathbf{x})}, q_1(\mathbf{x}) \right]$$

gives us the standard evolution equation

$$\frac{\partial}{\partial t} q_1(\mathbf{x}) = -[\psi_1(\mathbf{x}), q_1(\mathbf{x})],$$

and likewise for q_2.

From the above it is clear how to construct the HD-dynamics, SA-dynamics, and DSA-dynamics of Section 2.5.

4.2. Two-layer results

We consider the initial condition

$$q_1 = \mathrm{e}^{-(x^2+(y-0.25)^2)/2} \quad \text{and} \quad q_2 = -\mathrm{e}^{-(x^2+(y+0.25)^2)/2}, \tag{53}$$

for the potential vorticity in each layer, which is composed of two shifted Gaussian monopolar vortices with opposite sign. This initial condition is depicted in Fig. 32, with the left panel of positive vorticity corresponding to layer-1 and the right panel of negative vorticity corresponding to layer-2. For Dirac constraints we chose

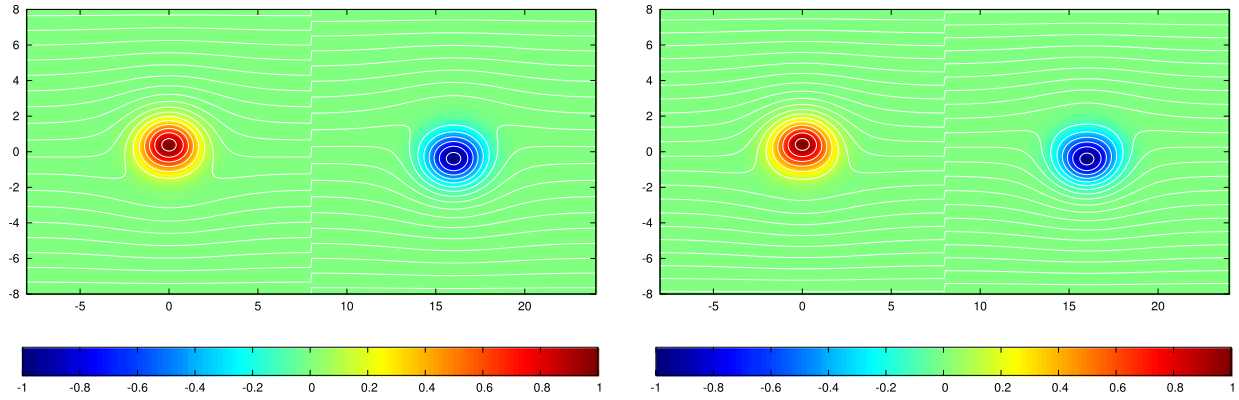

(a) $t = 20$. (b) $t = 50$.

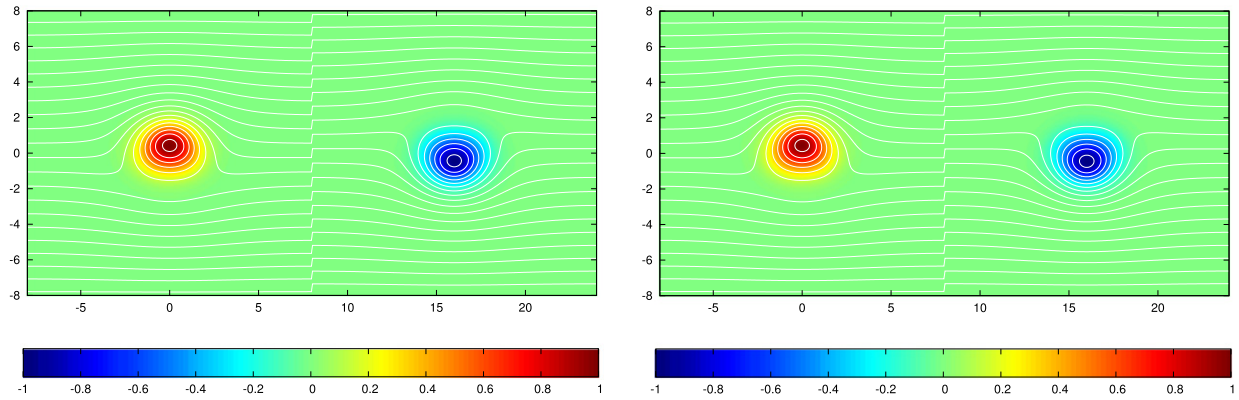

(c) $t = 120$. (d) $t = 150$.

Fig. 33. Vorticity (shading) and streamfunction (contours) under the two-layer version of DSA-dynamics of (40) with $\sigma = 0$, $\alpha = 1$, and the initial condition of (53) for the times shown.

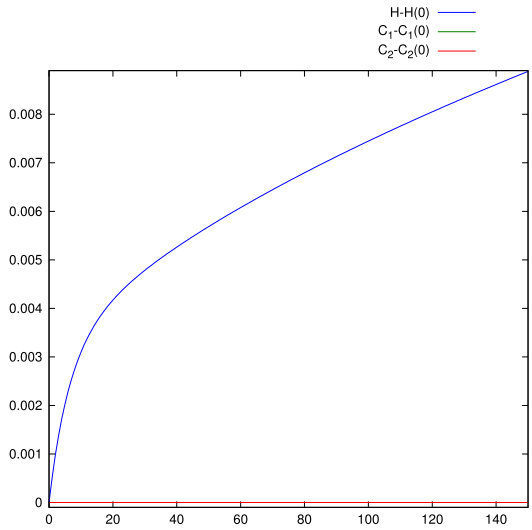

Fig. 34. The relative Hamiltonian H and Dirac constraints $C_1 = \mathcal{P}_x$ and $C_2 = S_p$ of (54) vs. time for the initial condition of (53), corresponding to the run of Fig. 33. The Dirac constraints remain nearly fixed as energy increases.

$C_1 = \mathcal{P}_x = \sum_{j=1,2} h_j P_x^j$, the total x-momentum and $C_2 = S_p$ given by

$$S_p = \frac{1}{k_0^2} \sum_{j=1,2} h_j \int_{\mathcal{D}} d\mathbf{x}\, \sin(k_0 x) \sin(k_0 y) q_j, \tag{54}$$

a quantity similar to the strain moment S, but superior in that it respects the periodic boundary conditions. Here $k_0 = 2\pi/L$ and we choose for our runs $h_1 = h_2 = 0.5$ and $\gamma = 1$.

Results for DSA-dynamics are depicted in Fig. 33, where it is seen that opposite signed monopoles persist in each layer as the dynamics proceeds. The structures maintain their integrity throughout the run, but the two structures change shape slightly as energy increases with the Dirac constraints nearly fixed in time. The numerical conservation property of the invariant C_2 is excellent, since it now matches the periodicity of the domain. This is evident from Fig. 34. These dipoles are smooth analogues of the states found in [31].

5. Conclusion

It is clear from the many examples considered that the method we propose is able to achieve its desired end. However, implementing this method numerically, though not difficult, can be rather delicate. In principle, the system should evolve to a local maximum of H on the constraint surface; however, since this is typically a saddle point in the infinite-dimensional function space without the constraints, slight errors can move the solution off the original surface and permit evolution toward a different maximum. For example, in the tripole experiments of Section 3.2, we often saw the vortex settle into a tripole state and then move off-center and form a circular vortex sitting on one of the zero lines of C_2, with the extra angular momentum appearing in the displacement of the center. The code was not able to preserve the symmetry, and the system ended up in a higher H state. By adding two more constraints, the components of the linear momentum, we prevented the symmetry breaking, but the vortex instead threw off vorticity into either spines or a band, so that the center still axisymmetrized. Thus, although the method can be made to work well, choosing constraints and initial conditions appropriately and running with high enough resolution are issues. On the plus side, we note that implementation

is straightforward because calculation of the effective streamfuctions (e.g. (34)) used for advection requires relatively minor modification of existing vortex codes.

It is obvious that many generalizations and additional applications are possible. Issues pertaining to the existence of solutions in quasigeostrophic dynamics for monopolar and dipolar states [32–37,28] would be a natural next set of applications. One could also pursue reduced magnetohydrodynamics, since it possesses a dynamics and Hamiltonian structure [38] similar to the vortex examples presented here, but with one additional scalar field that describes the magnetic field. Another possibility would be to implement the dual formulation of metriplectic dynamics [11]. For example, we could begin with the bracket [39]

$$\{F, G\}_\psi = \int_{\mathcal{D}} \mathrm{d}\mathbf{x}\, \psi \left[\frac{\delta F}{\delta q}, \frac{\delta G}{\delta q}\right], \tag{55}$$

which does not satisfy the Jacobi identity but does have the Hamiltonian as a null element, i.e. $\{H, G\}_\psi = -\int_{\mathcal{D}} \mathrm{d}\mathbf{x}\, \psi\, [\psi, \delta G/\delta q] \equiv 0$ for all G, and use (55) to construct the following 'entropy producing' symmetric bracket:

$$((F, G))_\psi = \int \mathrm{d}\mathbf{x}' \int \mathrm{d}\mathbf{x}'' \{F, q(\mathbf{x}')\}_\psi \mathcal{K}(\mathbf{x}', \mathbf{x}'') \{G, q(\mathbf{x}'')\}_\psi . \tag{56}$$

With $\mathcal{F} = H + C$ as the generator, this gives

$$\begin{aligned} \dot{q} &= \{q, \mathcal{F}\} + ((q, \mathcal{F}))_\psi = \{q, H\} + ((q, C))_\psi \\ &= [\psi, q] + [\Phi_\psi, \psi], \end{aligned} \tag{57}$$

where $\Phi_\psi(x) = \int_{\mathcal{D}} \mathrm{d}\mathbf{x}'\, \mathcal{K}(x, x')[\psi(x'), \mathcal{C}(q(\mathbf{x}'))]_{x'}$. By construction, $\dot{\mathcal{F}} = ((C, C))_\psi = \dot{C} \geq 0$, and thus this bracket maximizes C at fixed Hamiltonian or energy. It would be interesting to compare numerical implementation of this dual formulation with those presented.

As another possibility we mention that dissipation or driving can be included by adding a time dependence to the Hamiltonian by e.g. adding $H_{\mathrm{ext}} = \int_{\mathcal{D}} \mathrm{d}\mathbf{x}\, q(\mathbf{x}) \psi_{\mathrm{ext}}(\mathbf{x}, t)$ (cf. [40]). When this is done the noncanonical Poisson bracket will maintain the Casimir invariants, and perhaps one can use the added degree of freedom of ψ_{ext} to drive the system to a desired state.

Lou Howard's famous optimization paper [41] demonstrated how informative obtaining constrained bounds on fluid transport properties could be. In a similar vein, our paper provides a method for incorporating multiple constraints into conservative dynamical systems and approaches for modifying them to dissipate specific quantities while preserving others. We have not addressed many interesting issues, such as the relationship to linear and nonlinear stability, nor have we examined other kinds of dynamics such as those alluded to above, although we have every reason to expect that the approach herein will be applicable just as [13–15] have shown that SA-dynamics can be posed for a wide variety of systems. We believe that adding Dirac constraints allows the exploration of a much wider and richer variety of optimization problems.

Acknowledgements

GRF was supported by NSF grant #OCE-0752346, while PJM was supported by US Dept. of Energy Contract #DE-FG05-80ET-53088. Both would like to acknowledge multiple years of hospitality of the Geophysical Fluid Dynamics Summer School held at Woods Hole Oceanographic Institution.

References

[1] P.J. Morrison, J.M. Greene, Noncanonical Hamiltonian density formulation of hydrodynamics and ideal magnetohydrodynamics, Phys. Rev. Lett. 45 (1980) 790–793.
[2] P.J. Morrison, Poisson brackets for fluids and plasmas, in: M. Tabor, Y. Treve (Eds.), Mathematical Methods in Hydrodynamics and Integrability in Dynamical Systems, vol. 88, Am. Inst. Phys., New York, 1982, pp. 13–46.
[3] R. Salmon, Hamiltonian fluid mechanics, Annu. Rev. Fluid Mech. 20 (1988) 225–256.
[4] P.J. Morrison, Hamiltonian description of the ideal fluid, in: R. Salmon, B. Ewing-DeRemer (Eds.), 1993 Summer Study Program in Fluid Dynamics, vol. WHOI-94-12, Woods Hole Oceanographic Institution, 1993, pp. 16–110. http://hdl.handle.net/1912/545.
[5] T.G. Shepherd, Applications of Hamiltonian theory to GFD, in: R. Salmon, B. Ewing-DeRemer (Eds.), 1993 Summer Study Program in Fluid Dynamics, vol. WHOI-94-12, Woods Hole Oceanographic Institution, 1993, pp. 113–152. http://hdl.handle.net/1912/545.
[6] P.J. Morrison, Hamiltonian description of the ideal fluid, Rev. Modern Phys. 70 (1998) 467–521.
[7] A.N. Kaufman, Dissipative Hamiltonian systems: a unifying principle, Phys. Lett. A 100 (1984) 419–422.
[8] P.J. Morrison, Bracket formulation for irreversible classical fields, Phys. Lett. A 100 (1984) 423–427.
[9] M. Grmela, Bracket formulation of dissipative fluid mechannics equations, Phys. Lett. A 102 (1984) 355.
[10] F. Otto, The geometry of dissipative evolution equations: the porous medium equation, Comm. Partial Differential Equations 26 (2001) 101–174.
[11] P.J. Morrison, A paradigm for joined Hamiltonian and dissipative systems, Physica D 18 (1986) 410–419.
[12] R.W. Brockett, Dynamical systems that sort lists and solve linear programming problems, Proc. IEEE 27 (1988) 799.
[13] G.K. Vallis, G. Carnevale, W.R. Young, Extremal energy properties and construction of stable solutions of the Euler equations, J. Fluid Mech. 207 (1989) 133–152.
[14] G. Carnevale, G.K. Vallis, Pseudo-advection relaxation to stable states of inviscid two-dimensional fluids, J. Fluid Mech. 213 (1990) 549–571.
[15] T.G. Shepherd, A general method for finding extremal states of Hamiltonian dynamical systems, with applications to perfect fluids, J. Fluid Mech. 213 (1990) 573–587.
[16] P.J. Morrison, Thoughts on brackets and dissipation: old and new, J. Phys.: Conf. Ser. 169 (2009) 012006.
[17] P.J. Morrison, Hamiltonian and action principle formulations of plasma physics, Phys. Plasmas 12 (2005) 058102-1–058102-13.
[18] P.J. Morrison, Hamiltonian fluid mechanics, in: Encyclopedia of Mathematical Physics, vol. 2, Elsevier, 2006, pp. 593–600.
[19] E.C.G. Sudarshan, N. Makunda, Classical Dynamics: A Modern Perspective, John Wiley & Sons, New York, 1974.
[20] K. Sundermeyer, Constraint Dynamics, in: Lecture Notes in Physics, vol. 169, Springer Verlag, New York, 1982.
[21] P.J. Morrison, N.R. Lebovitz, J. Biello, The Hamiltonian description of incompressible fluid ellipsoids, Ann. Phys. 324 (2009) 1747–1762.
[22] P.J. Morrison, The Maxwell–Vlasov equations as a continuous Hamiltonian system, Phys. Lett. A 80 (1980) 383–386.
[23] P.J. Olver, A nonlinear Hamiltonian structure for the Euler equations, J. Math. Anal. Appl. 89 (1982) 233–250.
[24] M. Hirsch, S. Smale, Differential Equations, Dynamical Systems, and Linear Algebra, Academic Press, 1974.
[25] R. Courant, D. Hilbert, Methods of Mathematical Physics I, Wiley Interscience, New York, 1953.
[26] L. Kelvin, On the stability of steady and of periodic fluid motion, Phil. Mag. 23 (1887) 45–64.
[27] P. Rhines, W.R. Young, How rapidly is a passive scalar mixed within closed streamlines? J. Fluid Mech. 133 (1983) 133–145.
[28] D.G. Dritschel, On the persistence of non-axi-symmetric vortices in inviscid two-dimensional flows, J. Fluid Mech. 371 (1998) 141–155.
[29] G.S. Deem, N.J. Zabusk, Vortex waves: stationary "V states", interactions, recurrence, and breaking, Phys. Rev. Lett. 40 (1978) 859–862.
[30] H. Lamb, Hydrodynamics, Dover, New York, 1932.
[31] L.M. Polvani, Two-layer geostrophic vortex dynamics. Part 2. Alignment and two-layer V-states, J. Fluid Mech. 225 (1991) 241–270.
[32] G. Flierl, Baroclinic solitary waves with radial symmetry, Dyn. Atmos. Oceans 3 (1979) 15–38.
[33] G. Flierl, V.D. Larichev, J.C. McWilliams, G.M. Reznik, The dynamics of baroclinic and barotropic solitary eddies, Dyn. Atmos. Oceans 5 (1980) 1–41.
[34] J.C. McWilliams, G. Flierl, V.D. Larichev, G.M. Reznik, Numerical studies of barotropic modons, Dyn. Atmos. Oceans 5 (1981) 219–238.
[35] V.D. Larichev, G.M. Resnik, Two-dimensional Rossby soliton: an exact solution, Dokl. Akad. Nauk SSSR 231 (1976) 1077.
[36] V.D. Larichev, G.M. Resnik, Strongly nonlinear two-dimensional isolated Rossby waves, Oceanologia 16 (1976) 547–550.
[37] J.P. Boyd, Monopolar and dipolar vortex solitons in two space dimensions, Wave Motion 57 (1991) 223–243.
[38] P.J. Morrison, R.D. Hazeltine, Hamiltonian formulation of reduced magnetohydrodynamics, Phys. Fluids 27 (1984) 886–897.
[39] T.B. Benjamin, Impulse, flow force and variational principles, IMA J. Appl. Math. 32 (1984) 3–68.
[40] E. Tassi, P.J. Morrison, D. Grasso, F. Pegoraro, Hamiltonian four-field model for magnetic reconnection: nonlinear dynamics and extension to three dimensions with externally applied fields, Nucl. Fusion 50 (2010) 034007-1–8.
[41] L.N. Howard, Heat transport by turbulent convection, J. Fluid Mech. 17 (1963) 405–432.